

## *The intertidal hydraulics of tide-dominated reef platforms*

The Faculty of Oregon State University has made this article openly available.  
Please share how this access benefits you. Your story matters.

<b>Citation</b>	Lowe, R. J., Leon, A. S., Symonds, G., Falter, J. L., & Gruber, R. (2015). The intertidal hydraulics of tide-dominated reef platforms. <i>Journal of Geophysical Research: Oceans</i> , 120(7), 4845-4868. doi:10.1002/2015JC010701
<b>DOI</b>	10.1002/2015JC010701
<b>Publisher</b>	John Wiley & Sons, Inc.
<b>Version</b>	Version of Record
<b>Terms of Use</b>	<a href="http://cdss.library.oregonstate.edu/sa-termsfuse">http://cdss.library.oregonstate.edu/sa-termsfuse</a>

## RESEARCH ARTICLE

## The intertidal hydraulics of tide-dominated reef platforms

10.1002/2015JC010701

Ryan J. Lowe<sup>1,2,3,4</sup>, Arturo S. Leon<sup>5</sup>, Graham Symonds<sup>4,6</sup>, James L. Falter<sup>1,2,3,4</sup>, and Renee Gruber<sup>1,2,3,4</sup>

## Key Points:

- Hydrodynamics on a macrotidal reef investigated using field data and modeling
- Large water level asymmetries are well-predicted with a 1-D numerical model
- Analytical model predicts reef water depths based on morphology and roughness

## Correspondence to:

R. J. Lowe,  
Ryan.Lowe@uwa.edu.au

## Citation:

Lowe, R. J., A. S. Leon, G. Symonds, J. L. Falter, and R. Gruber (2015), The intertidal hydraulics of tide-dominated reef platforms, *J. Geophys. Res. Oceans*, 120, 4845–4868, doi:10.1002/2015JC010701.

Received 5 JAN 2015

Accepted 9 JUN 2015

Accepted article online 12 JUN 2015

Published online 14 JUL 2015

<sup>1</sup>School of Earth and Environment, University of Western Australia, Crawley, Australia, <sup>2</sup>ARC Centre of Excellence for Coral Reef Studies, University of Western Australia, Crawley, Australia, <sup>3</sup>The UWA Oceans Institute, University of Western Australia, Crawley, Australia, <sup>4</sup>Western Australia Marine Science Institution, Floreat, Australia, <sup>5</sup>School of Civil and Construction Engineering, Oregon State University, Corvallis, Oregon, USA, <sup>6</sup>CSIRO, Oceans and Atmosphere Flagship, Floreat, Australia

**Abstract** A 2 week field experiment investigated the hydrodynamics of a strongly tidally forced tropical intertidal reef platform in the Kimberley region of northwestern Australia, where the spring tidal range exceeds 8 m. At this site, the flat and wide (~1.4 km) reef platform is located slightly above mean sea level, such that during low tide the offshore water level can fall 4 m below the platform. While the reef always remained submerged over each tidal cycle, there were dramatic asymmetries in both the water levels and velocities on the reef, i.e., the flood duration lasted only ~2 h versus ~10 h for the ebb. These dynamics were investigated using a one-dimensional numerical model (SWASH) to solve the nonlinear shallow water equations with rapid (sub to supercritical) flow transitions. The numerical model revealed that as water drains off the reef, a critical flow point was established near the reef edge prior to the water discharging down the steep forereef. Despite this hydraulic control, bottom friction on the reef was still found to make a far greater contribution to elevating water levels on the reef platform and keeping it submerged over each tidal cycle. Finally, a simple analytical model more broadly shows how water levels on intertidal reef platforms functionally depend on properties of reef morphology, bottom roughness, and tidal conditions, revealing a set of parameters (a reef draining time-scale and friction parameter) that can be used to quantify how the water depth will fall on a reef during ebb tide.

## 1. Introduction

Circulation within coral reefs is primarily driven by wave and tidal forcing, and by a lesser extent wind and buoyancy forcing [see reviews by *Monismith*, 2007; *Lowe and Falter*, 2015]. Historically, most reef hydrodynamic studies have focused on the dynamics of wave-driven flows generated by wave breaking in the surf zone. This trend largely reflects the major geographical regions where investigators have chosen to work, such as in the Caribbean, the central North and South Pacific, and east and west Australia; locations where there is generally significant wave energy year round and tides are relatively small. These studies have greatly advanced our understanding of (1) wave transformation over shallow reefs [e.g., *Hardy and Young*, 1996; *Lugo-Fernández et al.*, 1998b; *Lowe et al.*, 2005; *Pomeroy et al.*, 2012; *Monismith et al.*, 2013], (2) the generation of wave setup through the surf zone [e.g., *Gerritsen*, 1980; *Gourlay*, 1996; *Jago et al.*, 2007; *Vetter et al.*, 2010], (3) the dynamics of wave-driven flows [e.g., *Symonds et al.*, 1995; *Hench et al.*, 2008; *Lowe et al.*, 2009b], and (4) the development of numerical models to predict these dynamics [e.g., *Lowe et al.*, 2009a; *Sheremet et al.*, 2011; *Roerber and Cheung*, 2012; *Van Dongeren et al.*, 2013].

The importance of tides on reef circulation is also well-recognized, particularly in the context of the relatively deep lagoons of barrier reefs and atolls [e.g., *King and Wolanski*, 1996; *Kench*, 1998; *Lowe et al.*, 2009a; *Dumas et al.*, 2012]. Tides have also been assessed for how they influence wave-driven hydrodynamics over shallow reefs, including the tidal modulation of wave energy transmission through reef surf zones [e.g., *Nelson*, 1994; *Hardy and Young*, 1996; *Lowe et al.*, 2005], tidal variations in wave setup [e.g., *Lugo-Fernandez et al.*, 1998a; *Bonneton et al.*, 2007; *Taebi et al.*, 2011; *Becker et al.*, 2014], and the influence of tides on depth-dependent bottom drag [e.g., *Pomeroy et al.*, 2012; *Monismith et al.*, 2013]. *Gourlay* [1996] and later *Gourlay and Colleter* [2005] (hereinafter GC05) also showed that, by controlling the relative depth over reefs, the tide can also establish two fundamentally distinct wave-driven flow regimes: (1) the more typical case, where resistance to the flow is provided by bottom drag forces (referred to as “reef top control”) and (2) a case

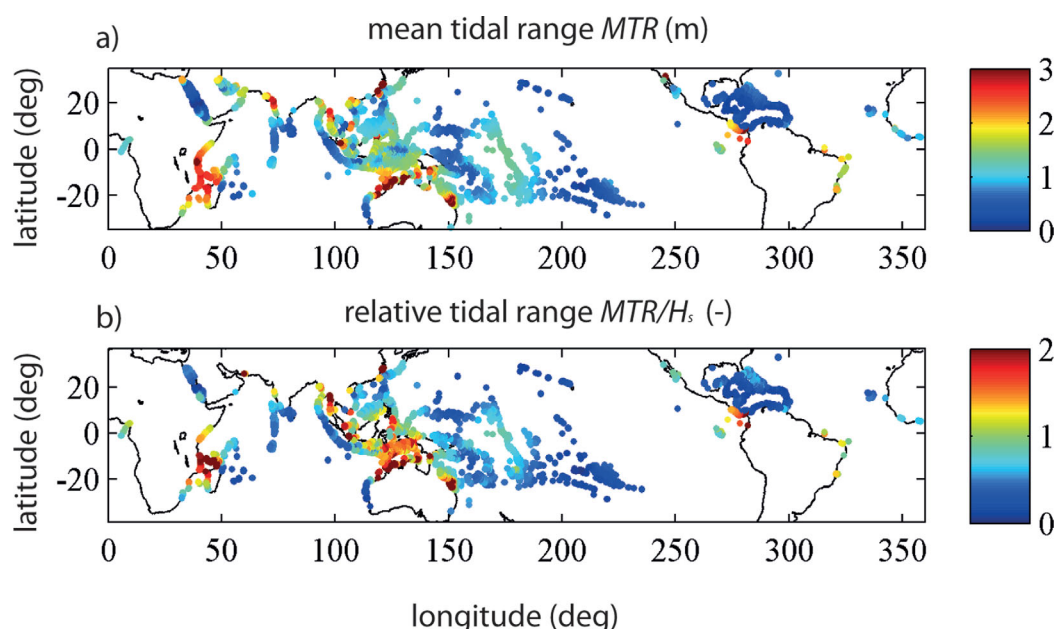


**Figure 1.** Global tidal ranges at coral reef sites worldwide. (a) The mean tidal range in meters ( $MTR$ ) and (b) the mean tidal range normalized by the annual mean significant wave height ( $MTR/H_s$ ) (figure adapted from *Lowe and Falter* [2015] with permission from the *Annual Review of Marine Science*, Volume 7 © 2015 by Annual Reviews, <http://www.annualreviews.org>).

where the water flowing off a reef can become supercritical when the offshore water level is near or below the reef platform height (referred to as “reef rim control”). Under reef rim control, a hydraulic control forms at the reef edge, which can allow the water level inside a lagoon to far exceed the water level offshore and limit the exchange of water between the lagoon and ocean [Callaghan *et al.*, 2006].

Unlike wave-dominated reef systems, where the offshore wave heights are comparable to or greater than the local tidal range, the hydrodynamics of “tide-dominated” reef platforms, where the tidal range far exceeds local wave heights, have yet to be studied in much detail. *Lowe and Falter* [2015] presented a global survey of the wave and tidal conditions experienced by coral reefs, and found that while wave-dominated reefs may be more abundant globally, roughly one-third of reefs worldwide experience a mean tidal range ( $MTR$ ) greater than the annual mean significant wave height ( $H_s$ ). Figure 1 shows that there are vast coral reef provinces globally that would be considered tide-dominated, such as along northern Australia, east Africa, the Pacific coast of Central America, and parts of Southeast Asia. Of these, a smaller subset would also be considered “macro-tidal” (i.e.,  $MTR > 3$  m). Unfortunately, the hydrodynamics of these macrotidal reefs also tend to be the most poorly studied globally. As a consequence, there remain major gaps in our understanding of the processes that control water level variability, circulation, and flushing of these strongly tidally forced reefs.

In this paper, we investigate the hydrodynamics of a macrotidal reef in northwestern Australia where the tidal range reaches  $\sim 8$  m during spring tide and wave forcing is negligible. The main goals of the study are: (1) to quantify the tidal circulation patterns throughout the reef, the asymmetries in the water levels and currents, and the implications for tidal flushing of these reefs; (2) to investigate the dominant momentum balances that are established across these reefs, and the relative importance of bottom friction versus the existence of a critical hydraulic control point in limiting the exchange of water between the reef and ocean; (3) to determine whether we can successfully simulate these complex, rapidly-varied flows through the development of numerical and analytical models; and (4) to use these models to more generally explore how circulation across tide-dominated reef platforms varies over a wider range of geomorphologies than our single field site can provide. For reference, Table 1 summarizes the variables used throughout the paper.

## 2. Methodology

### 2.1. Site Description

The field experiment was conducted in the Kimberley region of northwestern Australia (Figure 2a), where the tide is predominantly semidiurnal and the tidal range is among the largest anywhere in the world (over

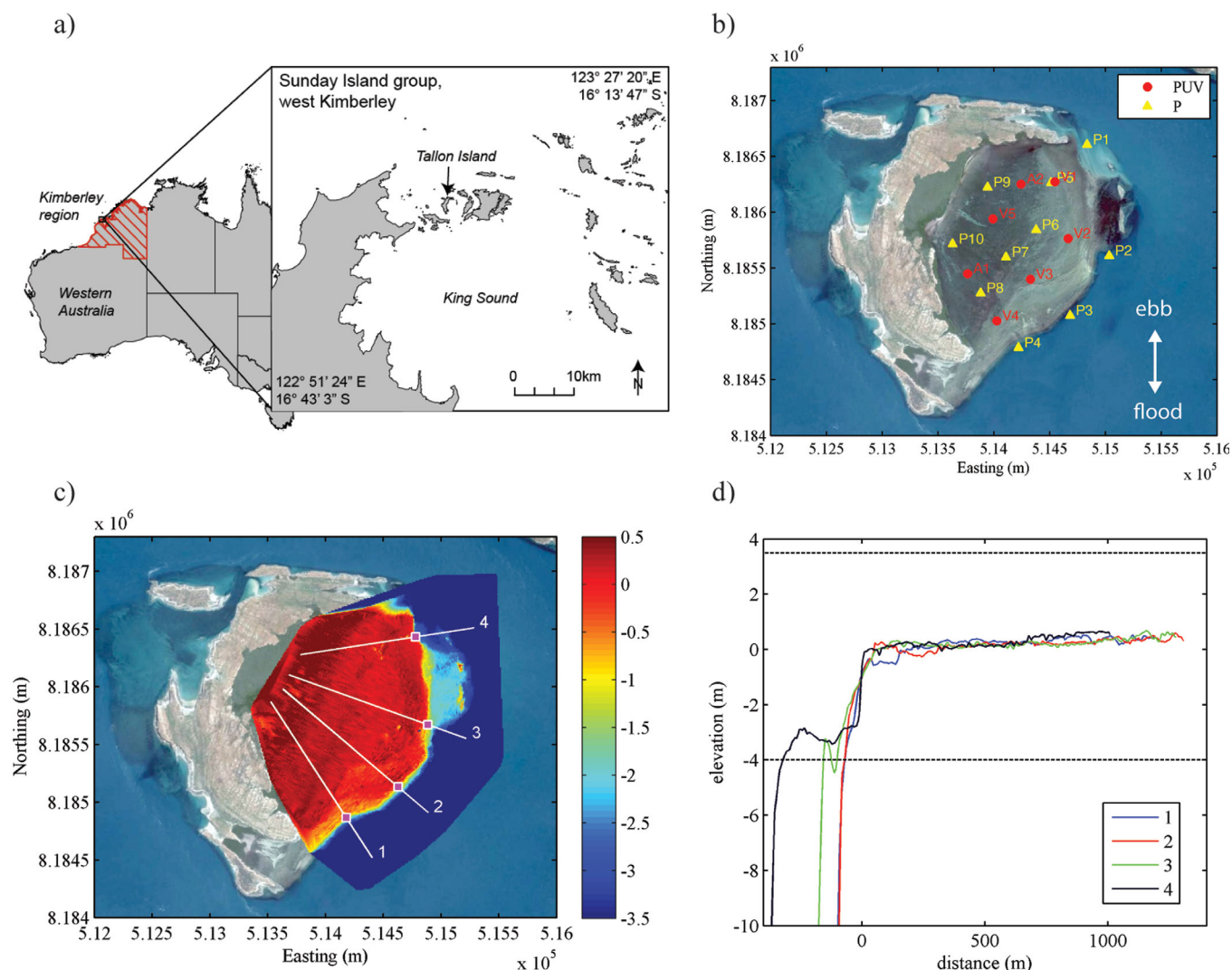


**Figure 2.** (a) The study site on Tallon Island, in the Kimberley region of northwestern Australia. (b) Aerial photograph of Tallon Island with the instrument sites superimposed. Red dots (PUV) sites denote acoustic Doppler velocimeters and profilers where both pressure and velocities were measured. Yellow triangles (P) denote locations where pressure sensors were deployed. The approximate flood and ebb current directions offshore from the island are denoted by the white arrows. (c) Bathymetry relative to mean sea level (in meter). The white lines denote four cross-reef transects, with the magenta squares highlighting the edge of the reef. (d) Bathymetry profiles across the four transects in Figure 2c, with the cross-reef distance relative to the reef edge (note that this distance is equivalent to  $L_r - x$ ). The horizontal-dotted lines bound the maximum and minimum water levels recorded at P1 during the experiment.

12 m in some locations; Kowalik [2004]). The study specifically targeted the intertidal reef platform on Tallon Island (16°24'S, 123°08'E) in the Sunday Island group. At this site, the spring tidal range can exceed 8 m and the reef is sheltered by surrounding islands such that wind waves (sea and swell) are negligible. Like other macrotidal reefs in this region, the reef rises abruptly out of deep water (>50 m depth) near the entrance to King Sound, and consists of a very flat reef platform that is far (>4 m) above the spring low tidal level (Figure 2d). Offshore of the reef edge (or "crest") is a steep foreereef that varies from nearly vertical (up to ~1:1) in northern parts to a slightly milder (but still steep) ~1:20 slope in the south (Figure 2d). When the water level falls below the crest at low tide, water discharges off the reef crest as a "waterfall" on the steepest sections (Figures 3a and 3b). Bathymetric surveys indicate that the reef platform is extremely flat (see below), with elevations varying by <0.3 m over its entire ~1400 m width. The average height of the platform is +0.1–0.3 m above mean sea level (MSL).

The benthic composition of the platform, and hence characteristics of the bottom roughness, can be divided into a few distinct zones across the reef (Figure 3e). A seaward zone extends ~300 m shoreward from the reef crest, and consists of a mostly coralline algal reef framework, interspersed with macroalgae



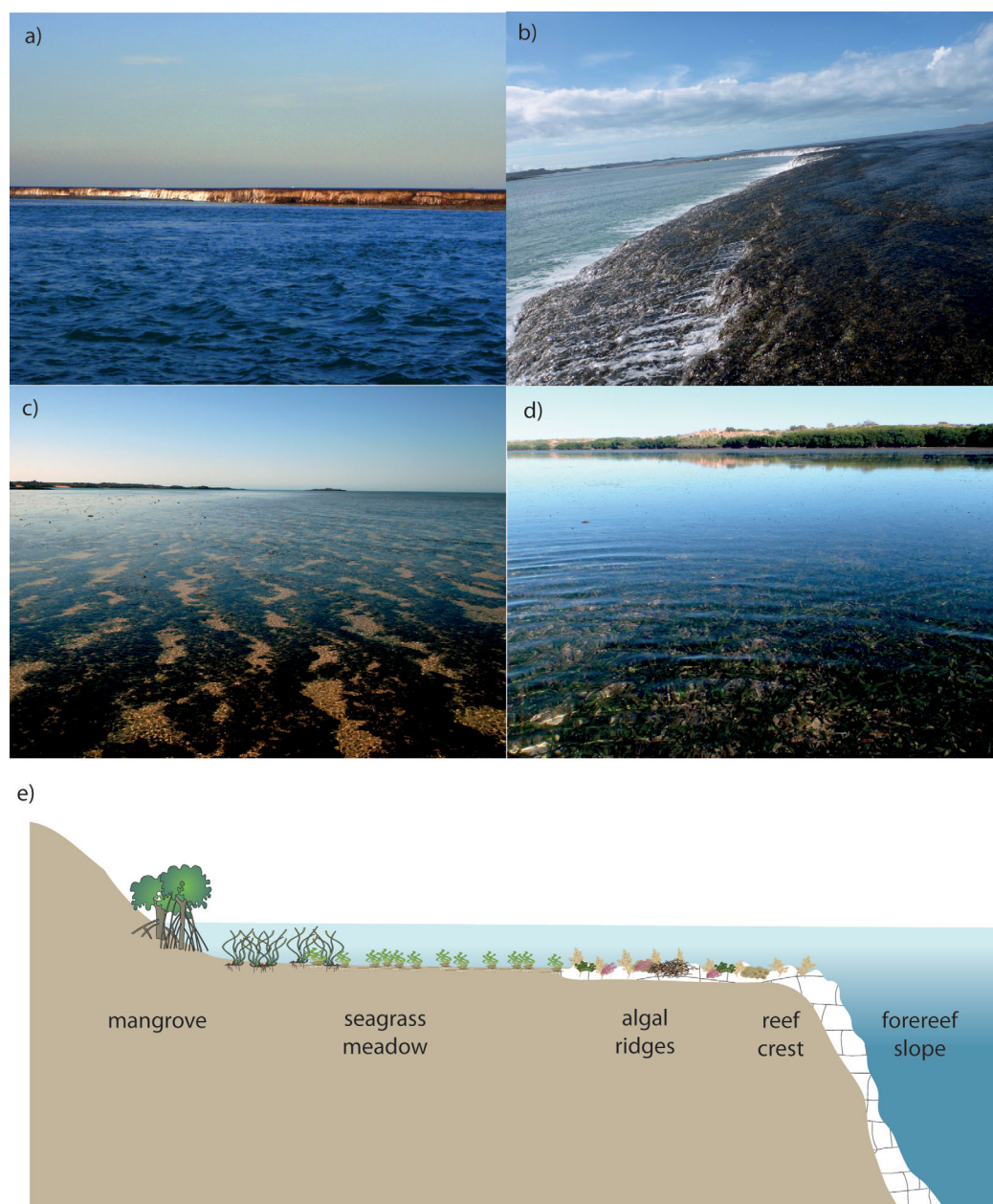


**Figure 3.** Reef zonation. Photographs of: (a) water draining off the reef crest as a waterfall at low tide, taken offshore at the steep northern section of the reef near transect 4 in Figure 2c; (b) water draining off the crest at the same location, but taken on top of the reef crest looking toward the south; (c) algal ridges running parallel to the reef (note that water drains off the reef to the right in the photo); and (d) a dense seagrass meadow at the platform with mangroves in the distance. (e) A schematic diagram of the different zones on the reef (refer to the text for details). Note that the vertical scale of the diagram is exaggerated.

and various macroinvertebrates, including some patches of coral colonies. In this zone, numerous ridges formed by coralline algae generally run parallel to the reef edge and contain sand and rubble in their troughs (Figure 3c). Substrate within the interior zone of the reef platform consists largely of sand and rubble populated with patches of seagrass that vary in shoot density (*Thalassia hemprichii*). Near the back of the reef, a denser meadow of a larger seagrass (*Enhalus acoroides*) dominates (Figure 3d). Finally, a continuous line of mangroves grows directly in front of the rocky island coastline. The benthic zonation we describe here for Tallon Island is also commonly found in many other reefs in the coastal Kimberley region [Purcell, 2002].

**Table 1.** Summary of Variables

Variable	Units	Description
$\alpha$		Fraction of the initial shoreline depth when a reef dries
$C_d$		Bottom drag coefficient
$Fr$		Froude number
$g$	$\text{m s}^{-2}$	Gravitational acceleration
$h$	m	Local water depth
$h_c$	m	Critical depth
$h_{max}$	m	Maximum depth at the shoreline
$h_n$	m	Normal depth
$H_s$	m	Significant wave height
$k_s$	m	Nikuradse bottom roughness length scale
$L_r$	m	Width of the reef platform
$MTR$	m	Mean tidal range
$MSL$	m	Mean sea level
$\vec{q}$	$\text{m}^2 \text{s}^{-1}$	Discharge vector
$q_{crest}$	$\text{m}^2 \text{s}^{-1}$	Discharge off the reef platform at the crest
$R_{cycle}$		Range of a tidal cycle
$S_0$		Local bed slope
$S_{0,FR}$		Forereef slope
$t$	s	Time
$t_{dry}$	s	Time when a reef dries
$T_{exp}$	s	Duration of the experiment
$T_d$	s	Reef draining time-scale
$T_{fall}$	s	Tidal fall duration
$T_{rise}$	s	Tidal rise duration
$T_{tide}$	s	Tidal period
$\vec{u}$	$\text{m s}^{-1}$	Depth-averaged current vector
$u$	$\text{m s}^{-1}$	Depth-averaged cross-reef velocity
$\forall$	$\text{m}^2$	Storage (volume) of water on the reef per unit width
$x$	m	Cross-reef distance measured from the shoreline ( $x=0$ m)
$z_b$	m	Bottom elevation measured relative to MSL (positive upward)
$\Phi_f$		Dimensionless friction parameter
$\Gamma$		Dimensionless constant ( $\approx 1.0$ )
$\eta$	m	Surface elevation measured relative to MSL
$\eta_{max}$	m	Maximum tidal amplitude relative to MSL
$\kappa$		Von Karman constant
$\rho$	$\text{kg m}^{-3}$	Seawater density
$\tau_b$	$\text{N m}^{-2}$	Bed stress

### 2.2. Field Experiment

A 2 week (25 March to 9 April 2014) field experiment was conducted where 17 hydrodynamic instruments recorded data continuously both on and off the reef platform (Figure 2b and Table 2). Ten RBR Virtuoso D|tide pressure sensors (denoted P1–P10) recorded water depths at four locations offshore of the reef (P1–P4), thus located below the minimum tidal level during the experiment, as well as at six sites distributed on the reef (P5–P10). Five flexible-head Nortek Vector acoustic Doppler velocimeters (sites V1–V5) were deployed on low profile tripods and continuously measured velocities and pressure; the Vector heads were mounted upward-looking such that the velocities were recorded  $\sim 0.4$  m above the bed. Finally, two 2 MHz Nortek Aquadopp profilers (ADPs) were deployed on the reef (sites A1–A2) and mounted upward-looking flush with the bottom. All instruments were synchronized to  $< 5$  s by comparing instrument clocks to a common reference before and after their deployment.

High-resolution bathymetry was obtained by surveying the reef with a small boat at high tide using an echosounder integrated with a Real Time Kinematic/Global Navigation Satellite System (RTK-GNSS) to remove the effects of tide (accuracy  $< 0.05$  m). However, the abundance of the large seagrass species (*Enhalus acoroides*) within the back 500 m of the reef most likely contributed to some small positive bias ( $\sim 0.2$ – $0.3$  m) in the measured elevations in this region. As the echosounder would likely detect the top of the seagrass canopy with leaf lengths  $\sim 0.3$  m, this can explain the slight shallowing of the bottom elevation  $z_b$  in Figure 2c that was not observed in the bottom-mounted pressure sensor data at these

back reef sites (Table 2). Overall, the elevations on the platform tend to fall within a remarkably narrow range of  $z_b = +0.1$ – $0.3$  m above MSL.

### 2.3. Data Analysis

All raw data were averaged at 1 min intervals onto a common time base. The pressure sensor data were converted to water depths after removing local atmospheric pressure variations and assuming a mean seawater density of  $\rho = 1025 \text{ kg m}^{-3}$ . To put all of the measurements of local water depth into a common vertical reference datum, we assumed that at slack high tide the sea surface was flat across the study area, then determined the relative depth offset between each site, and finally adjusted the data such that  $z = 0$  m corresponded to the mean water level of the experiment as measured offshore at site P3. This approach was deemed more accurate than relying on the RTK-GNSS boat survey data since the exact elevations of the instruments were not surveyed.

**Table 2.** Site Locations and Instrument Configurations<sup>a</sup>

Site	Zone	Easting (m)	Northing (m)	$z_b$ RTK (m)	$z_b$ Pressure (m)	Instrument	Sampling Information
V1	Reef crest	514546	8186273	+0.17	+0.06	Nortek Vector	2 Hz continuous, pressure sample height = 0.08 m, velocity sample height = 0.44 m
V2	Reef crest	514665	8185764	+0.18	+0.08	Nortek Vector	2 Hz continuous, pressure sample height = 0.08 m, velocity sample height = 0.44 m
V3	Reef crest	514326	8185401	+0.08	+0.04	Nortek Vector	2 Hz continuous, pressure sample height = 0.08 m, velocity sample height = 0.44 m
V4	Reef crest	514026	8185028	+0.14	+0.07	Nortek Vector	2 Hz continuous, pressure sample height = 0.08 m, velocity sample height = 0.44 m
V5	Back reef	513992	8185941	+0.23	+0.09	Nortek Vector	2 Hz continuous, pressure sample height = 0.08 m, velocity sample height = 0.44 m
A1	Mid reef	513765	8185450	+0.22	+0.12	Nortek Aquadopp HR	1 Hz continuous, pressure sample height = 0.05 m, blanking distance = 0.1 m; bin size = 0.03 m;
A2	Mid reef	514242	8186252	+0.09	+0.08	Nortek Aquadopp	Average currents every 300 s, pressure sample height = 0.08 m, blanking distance = 0.1 m; bin size = 0.1 m;
P1	Offshore	514836	8186605	-4.25	-4.41	RBR Virtuoso D tide	1 Hz continuous, pressure sample height = 0.05 m
P2	Offshore	515033	8185609	-7.05	-4.67	RBR Virtuoso D tide	1 Hz continuous, pressure sample height = 0.05 m
P3	Offshore	514682	8185076	-4.79	-4.79	RBR Virtuoso D tide	1 Hz continuous, pressure sample height = 0.05 m
P4	Offshore	514221	8184786	-8.17	-4.86	RBR Virtuoso D tide	1 Hz continuous, pressure sample height = 0.05 m
P5	Mid reef	514513	8186264	+0.04	N/A	RBR Virtuoso D tide	FAILED
P6	Mid reef	514379	8185843	+0.05	+0.27	RBR Virtuoso D tide	1 Hz continuous, pressure sample height = 0.05 m
P7	Mid reef	514108	8185597	+0.22	+0.30	RBR Virtuoso D tide	1 Hz continuous, pressure sample height = 0.05 m
P8	Mid reef	513882	8185278	+0.31	+0.31	RBR Virtuoso D tide	1 Hz continuous, pressure sample height = 0.05 m
P9	Back reef	513945	8186225	+0.49	+0.21	RBR Virtuoso D tide	1 Hz continuous, pressure sample height = 0.05 m
P10	Back reef	513632	8185714	+0.48	+0.22	RBR Virtuoso D tide	1 Hz continuous, pressure sample height = 0.05 m

<sup>a</sup>Coordinates are expressed in UTM zone 51K. “ $z_b$  RTK” represents the estimated bottom elevation  $z_b$  relative to MSL from the RTK survey for each instrument site (note that positive values indicate the bottom is above MSL). “ $z_b$  Pressure” denotes the bottom elevation estimated by the pressure sensors assuming the ocean surface is flat at peak (slack) high tide.

The raw Vector data were initially filtered with a minimum correlation threshold and despiked based on algorithms from *Goring and Nikora* [2002]. Data were also removed if the water surface was close to or below the velocity sample height, which we determined separately by comparing the echo amplitude signal and the water depth inferred by the pressure sensor (i.e., velocities could not typically be measured when the depth was  $\leq 0.5$  m). Note that the Vectors were located in slightly recessed patches of sand so that we could reliably measure velocities even when the depth over the surrounding reef decreased to  $\sim 0.3$ – $0.4$  m. For most Vectors, the water depth remained above this threshold over the full tidal cycle; however, on occasion sites V1 and V4 dropped below this depth.

For the standard Aquadopp (A2), the primary 5 min averaged current data were used as recorded and linearly interpolated onto the finer 1 min common time base defined by the Vector time series. Similarly, the raw 1 Hz Aquadopp HR or “High Resolution” (A1) data were also collected in 5 min-averaged bursts and then interpolated onto the Vector time base. Note that for consistency with the Vector data, where velocities were measured at a fixed height above the bed, the currents reported from the ADPs reflect measurements made at a similar height (specifically by averaging the bins between 0.2 and 0.4 m above bed). Similar to the Vector data processing, data recorded at heights near or above the surface by the ADPs were removed from the analysis.

### 3. Field Observations

#### 3.1. Water Levels

Observations of the water level ( $\eta$ ) variability (measured relative to the MSL) reveal that the tidal range reached a spring maximum of  $\sim 7.5$  m offshore (P1) near the middle of the study and a neap minimum of  $\sim 3$  m around both the beginning and end of the study (Figure 4a). In contrast, tidal variations at a representative site on the reef (P9) were substantially reduced, varying between  $\sim 3$  m during spring tide to only  $\sim 1.5$  m during neap tide.

Figures 4b and 4c shows a comparison of the water levels between the sites for a single representative spring tidal cycle; the general trends were similar among the other tidal cycles, differing only in magnitude. During the final part of the flood tide and initial part of the ebb (i.e.,  $-2$  hr  $< t < +2$  hr), the reef water levels

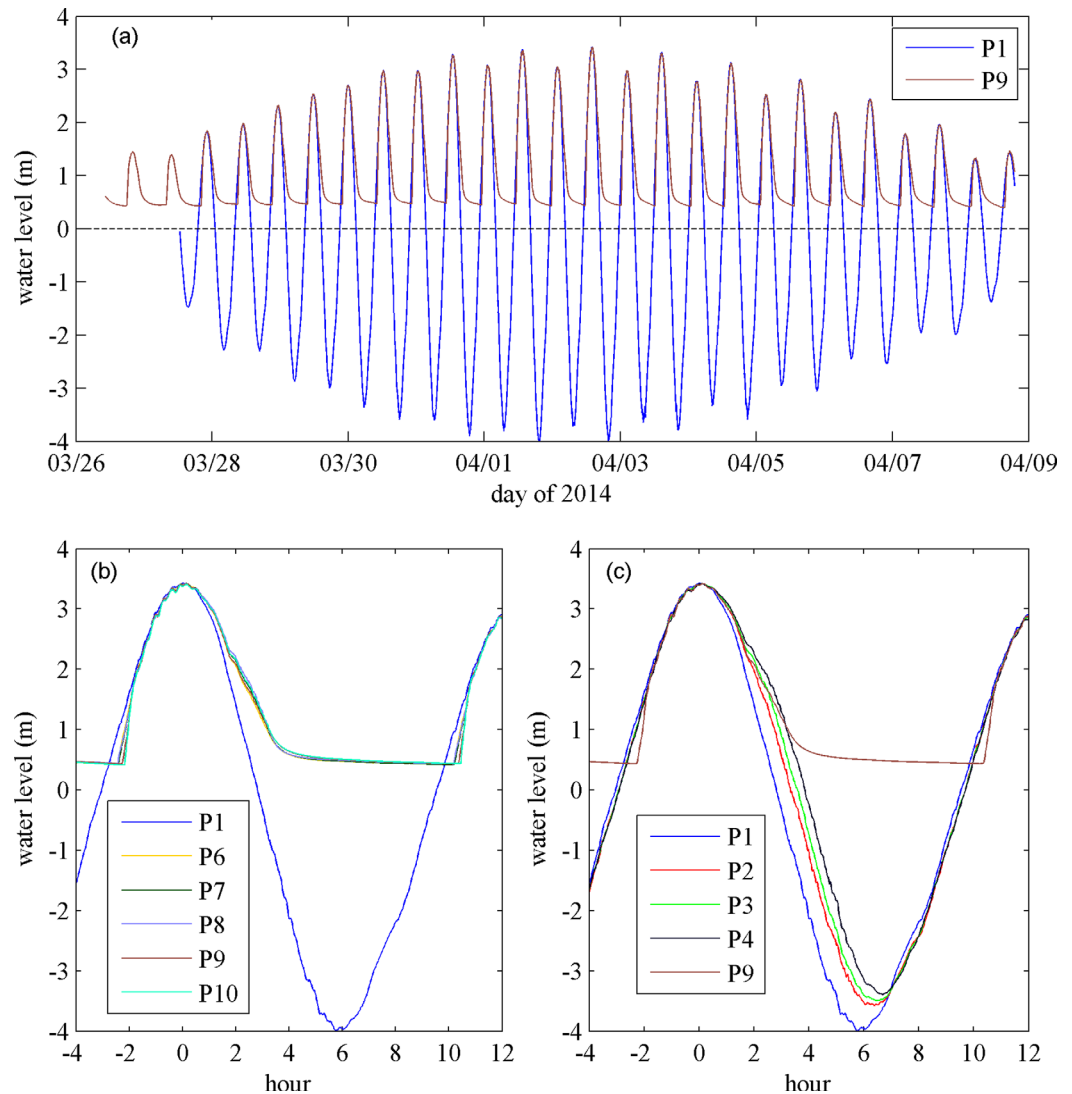


**Figure 4.** Water level variability. (a) Water level variations at a representative site offshore (P1) and on the reef platform (P9) for the entire experiment. For a single tidal cycle on 2 April, (b) the water levels measured at all pressure sensor sites on the reef (P6–P10) relative to offshore (P1), and (c) measured at all offshore sites (P1–P4) relative to on the reef (P9). Note that in Figures 4b and 4c time is defined relative to peak high tide when  $t = 0$  h.

closely matched the offshore levels; however, after  $t \gtrsim +2$  hr water drained much slower off the reef, resulting in a highly asymmetric tide (Figure 4b). For  $t \approx +2$ –4 h the reef water level fell at  $\sim 1.0 \text{ m h}^{-1}$  versus  $\sim 1.8 \text{ m h}^{-1}$  offshore; however, later ( $t > +5$  h) the water level fell at a rate of only  $\sim 0.1 \text{ m h}^{-1}$ . During the flood tide, there was a 1 h period where the offshore water level was initially up to 1 m higher than on the reef due to the delay in the tide propagating across the shallow and rough reef. Over this period, the water level rose much more rapidly on the reef until it roughly matched the offshore water level at  $\sim 3$  h before the peak high tide.

These substantial differences between offshore and reef water levels are analogous to the tidal distortions that are sometimes observed in strongly tidally forced estuaries. While tidal duration asymmetries can arise from a number of mechanisms [Nidziko and Ralston, 2012], the analogous mechanism here is the so-called “tidal truncation” effect where residual water draining from the intertidal zone of an estuary increases the fall duration [Lincoln and Fitzgerald, 1988]. Analysis of the full water level record ( $\sim 25$  individual cycles) reveals that on average the fall duration was  $T_{fall} = 6.1$  h for offshore sites (thus roughly half of the dominant  $\sim 12$  h semidiurnal tide), but averaged  $T_{fall} = 10.0$  h for sites on the reef (Table 3).



**Table 3.** Tidal Water Level Properties Recorded by the Pressure Sensor Array (P1–P10), Showing the Mean, Maximum, and Minimum Range of Each Tidal Cycle<sup>a</sup>

Site	Range (m) (mean)	Range (m) (max/min)	$T_{rise}$ (h)	$T_{fall}$ (h)
P1	5.9	7.6 / 3.3	6.58 ± 0.17	5.73 ± 0.20
P2	5.6	7.2 / 3.3	6.25 ± 0.13	6.08 ± 0.18
P3	5.5	7.3 / 3.3	6.12 ± 0.13	6.20 ± 0.19
P4	5.5	7.3 / 3.3	6.00 ± 0.18	6.32 ± 0.20
P6	2.3	3.0 / 1.4	2.47 ± 0.16	9.87 ± 0.30
P7	2.3	3.0 / 1.4	2.49 ± 0.44	9.85 ± 0.38
P8	2.3	3.0 / 1.4	2.35 ± 0.17	9.98 ± 0.27
P9	2.3	3.0 / 1.4	2.30 ± 0.19	10.05 ± 0.28
P10	2.3	3.0 / 1.4	2.16 ± 0.32	10.23 ± 0.29

<sup>a</sup> $T_{rise}$  and  $T_{fall}$  denote the rise and fall duration of each tidal cycle, respectively (mean ± std).

Figure 4c highlights differences between the offshore water level time series at sites along the reef (P1–P4). For these sites, the water levels were in close agreement during the flood tide. However, the water levels were slightly lagged from P1 to P4 during the ebb tide. This likely reflects the effect of island blocking, with the sites from P1 to P4 being increasingly located upstream of the island relative to the ebb direction of the tide exiting King Sound (Figure 2b). This led to a

modest along-reef water level gradient when the offshore water levels were still above the reef crest during the start of the ebb (Figure 4c).

The along-reef gradients were estimated from the water level differences from V1 and P8 along the reef, whereas cross-reef gradients were estimated from the difference between V1 and P9 (Figure 5). This reveals that the along-reef water level gradients were negligible over most of the tidal cycle, except for a brief period  $t \approx +1$ – $3$  h following high tide (Figure 5) when it mirrored the trend in the along-reef gradient observed offshore (Figure 4c). Nevertheless, for this representative tidal cycle, the magnitude of the along-reef water level gradients were still at most  $\sim 30\%$  of the cross-reef gradients, indicating that the dominant momentum balances should be oriented in the cross-reef direction for most of the tidal cycle.

### 3.2. Circulation

To investigate how the circulation varied on the reef during each tidal cycle, the velocity records were conditionally sampled based on the phase of the offshore tide (P1) and then phase-averaged over all tidal cycles (Figure 5). At all sites, there was a substantial asymmetry between the ebb and flood currents, both in magnitude and duration. During the ebb phase, the maximum flow speed tended to peak 2–3 h after high tide, but this lag increased slightly from north to south along the reef (i.e., from V1 to V4). The ebb flow also tended to be stronger at northern parts of the reef (i.e., V1 and V2 versus V3 and V4). Roughly 4 h after the peak high tide, the water drained slowly off the reef with speeds  $< 0.2 \text{ m s}^{-1}$ . During the flood phase, the maximum flow occurred within 1 h after the water level rose above the reef edge (i.e., at  $t \approx +10$  h; Figure 4). The duration of this flood was much shorter than the ebb. The magnitude of the maximum flood current relative to the maximum ebb current varied among the sites, and was either slightly weaker or stronger.

Tidally averaged current vector fields at different phases of the tide are shown in Figure 6. During the initial  $\sim 2$  h after high tide, the flow tended to be northwestward throughout the reef with most of the discharge occurring at the northern section (Figures 6b–6d). This northward flow is consistent with the along-reef component of the water level gradient that was present during the initial ebbing of the tide (Figure 5b). After  $t \approx +2$  h, when offshore water levels dropped below the reef edge, the along-reef pressure disappeared on the reef platform despite being present offshore, and the flow drained more uniformly off the reef (i.e., the flow vectors became directed roughly normal to the orientation of the reef edge). This slow draining ebb period lasted until  $t \approx +10$  h when the tide flooded the reef platform, and the flow became uniformly oriented in the cross-reef direction along the entire reef.

The asymmetries in the magnitude, duration, and spatial pattern of the tidal flows generated a residual circulation on the reef every tidal cycle. To quantify this residual transport, for each site we computed the time-averaged discharge vector  $\langle \vec{q} \rangle$ , defined as

$$\langle \vec{q} \rangle = \frac{1}{T_{\text{exp}}} \int_0^{T_{\text{exp}}} \vec{q} dt, \tag{1}$$

$$\vec{q} \equiv \int_0^h \vec{u} dz, \tag{2}$$

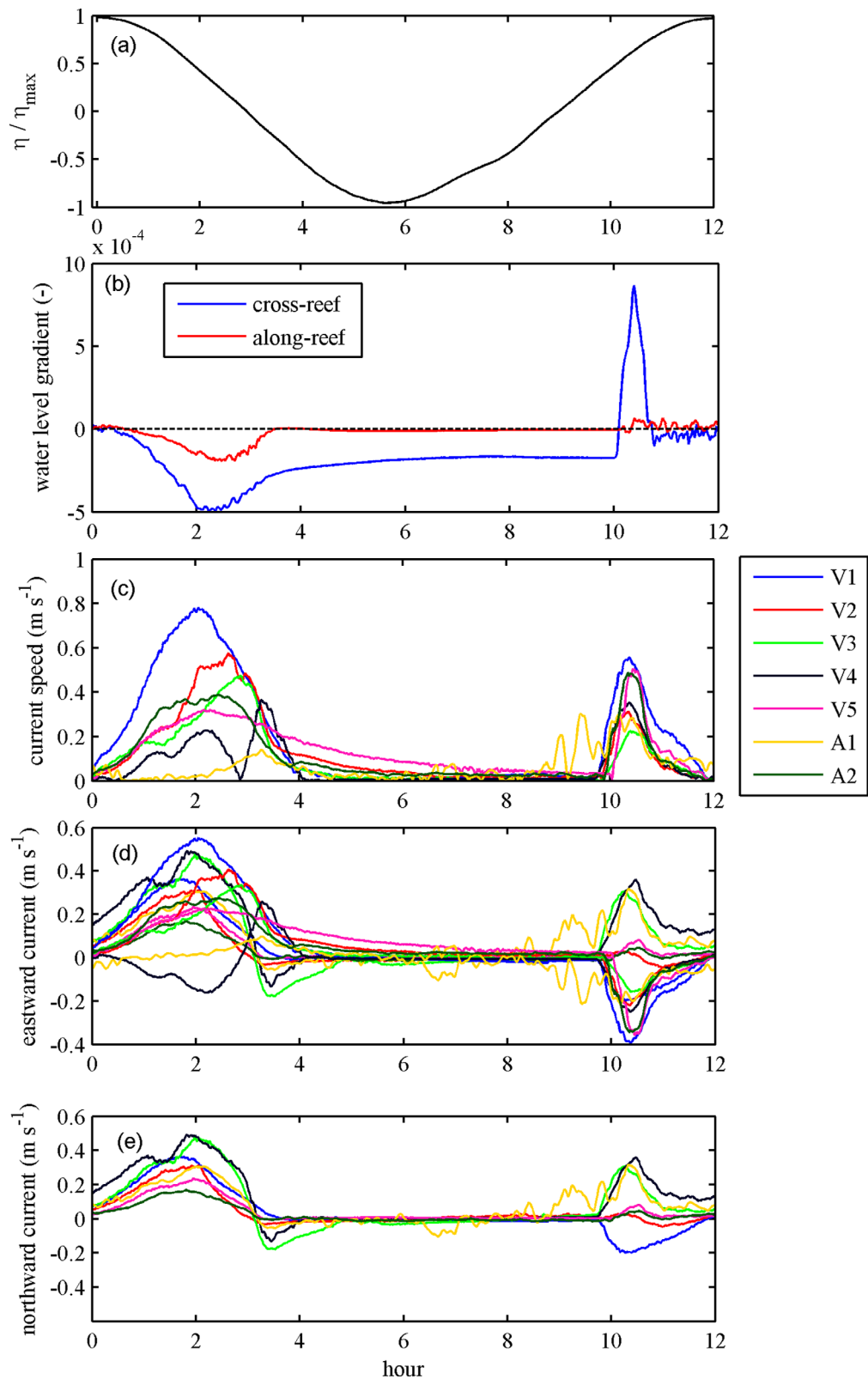


**Figure 5.** Water level gradient and tidal current variability on the reef. (a) The reference offshore tidal elevation  $\eta$  at P1 normalized by the maximum amplitude  $\eta_{\max}$ . (b) Cross and along-reef water level gradients for the same period as in Figures 4b and 4c. The cross-shore gradient is estimated from the water level difference between V1 and P9. The along-reef gradient is estimated from the water level difference between V1 and P8. (c)–(e) The tidal phase-averaged (c) current speed, and (d) eastward and (e) northward current vector components.

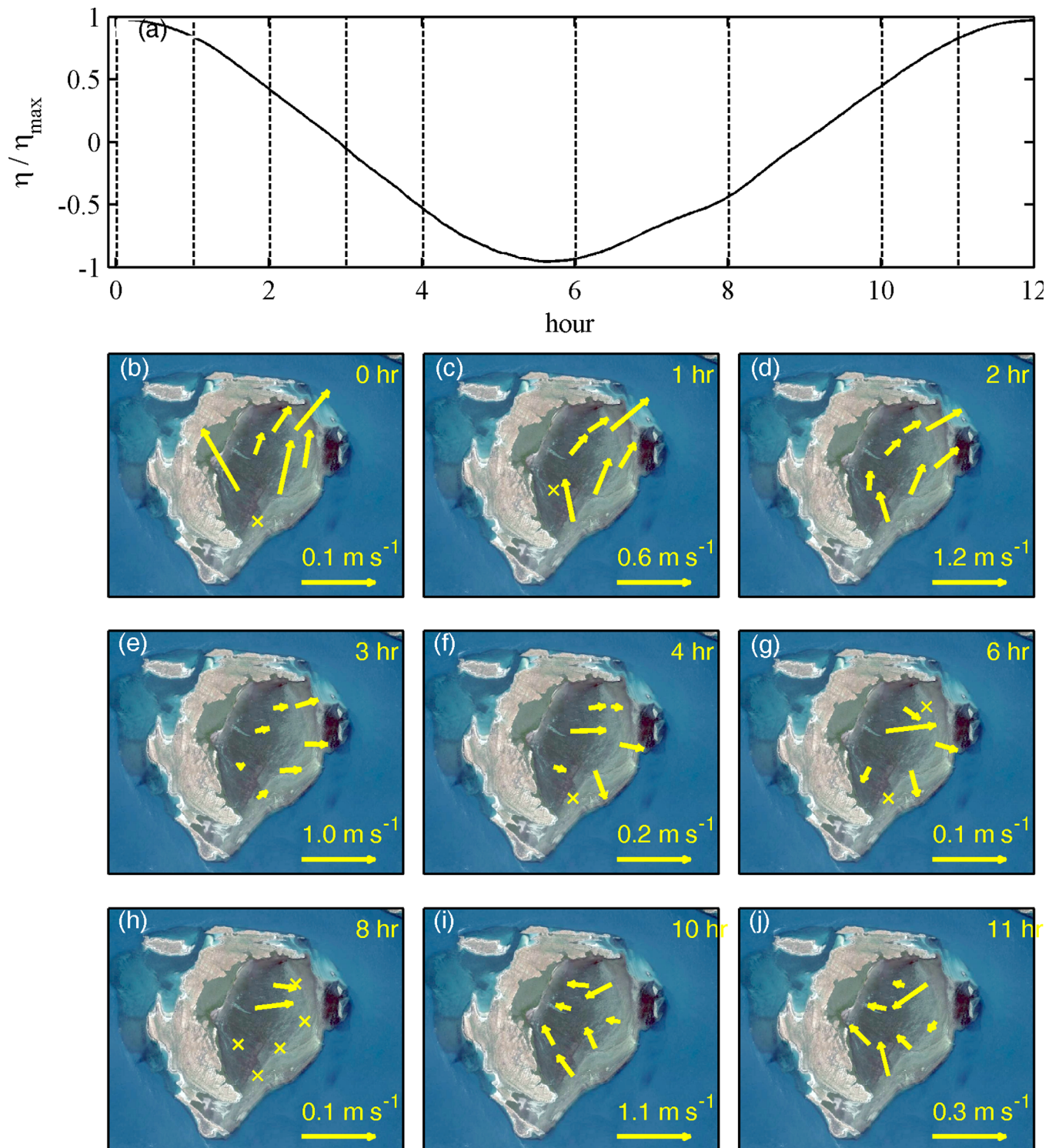


**Figure 6.** Tidal current vector fields on the reef at select phases of the tide. (a) For reference, the tidal phased-average offshore water level at P1, normalized by the mean tidal range. Vertical-dotted lines denote the select phases of the tide plotted in Figure 6b–6j. Tidal phase-averaged current vectors at select phases of the tide, referenced to the time of peak high tide ( $t=0$ ); (b) 0 h; (c) 1 h; (d) 2 h; (e) 3 h; (f) 4 h; (g) 6 h; (h) 8 h; (i) 10 h; and (j) 11 h. Note that the current vectors are scaled substantially among figures to emphasize the current patterns when the flow is relatively weak (refer to the reference current vector for scaling differences). The “x” symbols represent either flow speeds  $<0.01 \text{ m s}^{-1}$  or when the water was too shallow to measure flow.

where  $\vec{q}$  and  $\vec{u}$  are the discharge and current vectors, respectively,  $h$  is the local water depth, and  $T_{exp}$  denotes the experiment duration. Figure 7 reveals a residual  $|\langle \vec{q} \rangle| = 0.1\text{--}0.2 \text{ m}^2 \text{ s}^{-1}$  was present toward the northeast, leading to a net onshore component of the residual flow along the southern edge of the reef and an offshore

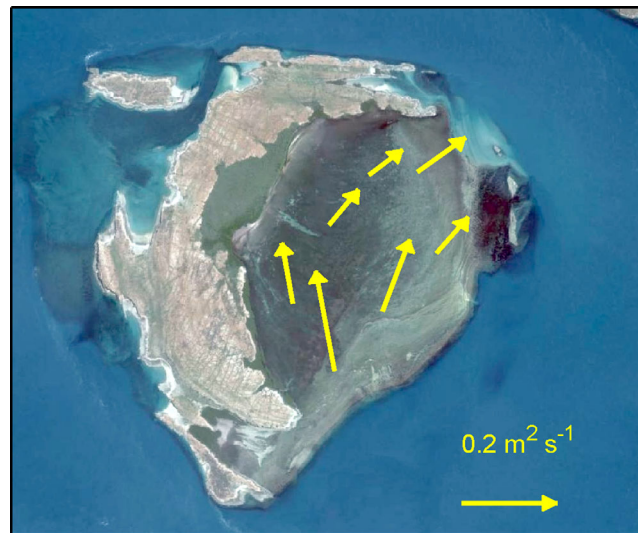


**Figure 7.** Residual discharge  $\langle \bar{q} \rangle$  computed for the duration of the experiment.

component along the northern edge. This net northward residual flow primarily arose from the northward flow that occurred on the reef for a relatively short ( $\sim 2$  h) period directly after high tide (Figures 6b–6d). This corresponds to  $\sim 10$ – $20\%$  of the average maximum flow  $q_{max}$  observed over the tidal cycle at each site (Table 3). We can also compute the residual discharge for each individual tidal cycle  $i$  (denoted  $\langle \bar{q} \rangle_i$ ) by integrating from peak-to-peak high tides (not shown). For each tidal cycle,  $\langle \bar{q} \rangle_i$  was strongly correlated with the tidal range of each offshore tidal cycle  $R_{cycle,i}$  (Table 4).

## 4. Reef Hydraulics

### 4.1. Governing Equations

To further investigate the reef hydrodynamics, we consider the simple one-dimensional (1-D, cross-reef) time-varying mass and momentum balances across the reef. Although there is a short period of  $\sim 2$ – $3$  h where two-dimensional (2-D) effects on circulation cannot be entirely neglected, the along-reef pressure gradients during this period were still  $< 30\%$  of the cross-reef gradients (Figure 5b). Therefore, assuming a 1-D cross-reef momentum balance over the full tidal cycle is reasonable and greatly reduces the complexity of the problem. On this basis, we use the depth-integrated 1-D nonlinear shallow water equations to investigate the hydrodynamics. Thus, from mass conservation

$$\frac{\partial h}{\partial t} + \frac{\partial (uh)}{\partial x} = 0, \quad (3)$$

and from momentum conservation

$$\underbrace{\frac{\partial u}{\partial t}}_{\text{acceleration}} + \underbrace{\frac{\partial}{\partial x} \left( \frac{u^2}{2} \right)}_{\text{advection}} + \underbrace{g \frac{\partial h}{\partial x}}_{\text{water depth gradient}} + \underbrace{\frac{\tau_b}{\rho h}}_{\text{bed stress}} + \underbrace{g \frac{\partial z_b}{\partial x}}_{\text{bed slope}} = 0, \quad (4)$$

where  $u$  is the depth-averaged velocity,  $\tau_b$  is the bed stress, and  $z_b$  is the bed level measured positive upward from MSL (i.e.,  $\eta = h + z_b$ ).

**Table 4.** Properties of the Residual Flow<sup>a</sup>

Site	$\langle \bar{q} \rangle$		$ \langle \bar{q} \rangle /q_{max}$	$r_{res,tide}$	$\langle \bar{q} \rangle_{cycle} = mR_{cycle} + q_0$	
	mag ( $m^2 s^{-1}$ )	dir (deg)			$m$ ( $m s^{-1}$ )	$q_0$ ( $m^2 s^{-1}$ )
V1	0.12	54	0.11	0.82	0.03	-0.07
V2	0.10	42	0.15	0.92	0.03	-0.05
V3	0.16	21	0.18	0.96	0.04	-0.07
V4	0.21	349	0.23	0.98	0.05	-0.11
V5	0.10	40	0.17	0.90	0.02	-0.05
A1	0.13	350	0.23	0.67	0.03	-0.06
A2	0.09	53	0.14	0.94	0.02	-0.03

<sup>a</sup> $\langle \bar{q} \rangle$  denotes the magnitude (mag) and direction (dir) of the residual discharge vector.  $r_{res,tide}$  denotes the correlation between the residual discharge  $\langle \bar{q} \rangle$ , and the tidal range  $R_{cycle,i}$  computed for each tidal cycle  $i$ .  $m$  and  $q_0$  denote the slope and intercept, respectively, of the linear regression between  $\langle \bar{q} \rangle_{cycle}$  and  $R_{cycle}$ .

### 4.2. Numerical Model

To numerically solve equations (3) and (4), we use the open-source model SWASH (Simulating WAVes till SHore) detailed in Zijlema *et al.* [2011]. While this code was designed to study the dynamics of wind waves, it is equally well suited for simulating the rapidly varied tidal flows in the present study. Most importantly, the numerical solution of the nonlinear shallow water equations is based on Stelling and Duijnmeijer [2003], which is designed to accurately simulate rapid flow transitions. In particular, SWASH is capable of



simulating transitions from supercritical to subcritical flow (i.e., hydraulic jumps) in open channel flow applications [Zhou and Stansby [1999], Zijlema et al. [2011] (see section 5.5 in that paper)], and flow over broad-crested weirs [e.g., Stelling and Duinmeijer [2003] based on our own testing]. We note that the latter broad-crested weir problem has strong analogies to the present reef application.

Given the very flat and uniform elevation of the reef platform (Figure 2d), we used a simplified reef profile that included a horizontal reef flat of width  $L_r = 1400$  m and a linear sloping forereef. The reef platform was assumed to be a constant  $z_b = +0.3$  m above MSL based on the spatially averaged bathymetry from the surveys. While the forereef slope varies somewhat along Tallon Island, we chose an average, representative slope of 1:5 for all simulations. Initial simulations during testing revealed that the solutions were largely insensitive to slopes ranging from at least 1:1 to 1:20 (not shown), which is also consistent with the analytical theory detailed in section 5. A 50 m deep, flat basin was located offshore of the forereef slope and extended 1000 m offshore. For all simulations, a fine horizontal grid resolution of 0.25 m was used. A wall boundary condition was applied at the shoreward edge of the reef (i.e., zero discharge) and a time varying water level boundary condition offshore. The offshore water level was forced by the measured water level time-series based on the average of all offshore sites (P1–P4). The momentum equations were solved with a first-order upwind scheme in SWASH (higher-order schemes were found to not improve the results yet were computationally less efficient). The numerical time integration was based on an implicit Euler scheme.

Bottom stresses can be parameterized using a few different approaches within SWASH; however, the simplest uses a quadratic friction law with a constant bottom drag coefficient  $C_d$  that is depth invariant, i.e.,

$$\tau_b = \rho C_d |u|u. \quad (5)$$

A number of reef studies have shown that the relative water depth over reef roughness can also modify the effect of bottom friction [e.g., McDonald et al., 2006; Pomeroy et al., 2012]. Both the Manning and logarithmic quadratic friction formulations include such a depth dependency. Initial model testing using each formulation revealed that both can reproduce the observations with comparable skill, so in the present study we opted to use the logarithmic formulation. When integrating a logarithmic velocity profile over the water column and relating it to the depth-averaged flow  $u$ ,  $C_d$  becomes depth-dependent according to:

$$C_d = \left[ \frac{\kappa}{\ln(30h/k_s) - 1} \right]^2. \quad (6)$$

Here  $k_s$  is an equivalent Nikuradse bottom roughness length scale, which is related to the physical length scales of the bottom roughness. While an equivalent  $k_s$  on natural reefs is usually difficult to define, many field studies have found it ranges between order 0.1 m and 1 m on reefs [Lowe et al., 2009a]. Likewise,  $C_d$  on reefs generally falls within a narrower range of order 0.01 when  $h/k_s \gg 1$  [Lowe and Falter, 2015].

Simulations were conducted with both the constant drag and logarithmic formulations and compared with the observations. We thus treated  $C_d$  and  $k_s$  partially as constrained calibration parameters and specifically quantified the model performance over a range of values from zero to a maximum value ( $C_d = 0.5$  and  $k_s = 1.0$  m). Quantitative measures of model performance were assessed by comparing the simulated and observed water levels on the reef platform by computing both the root-mean-squared (rms) error and the model “skill” [Willmott, 1982; see also Lowe et al., 2009a], where the model skill varies from 0 (complete disagreement) to 1 (complete agreement).

### 4.3. Numerical Results

Model simulations with bottom friction substantially improved predictive skill. For the constant  $C_d$  formulation, there was excellent agreement between the predicted and observed water levels on the reef for  $C_d = 0.02$  (Figure 8). Similarly, for the logarithmic formulation, the best agreement occurred when  $k_s = 0.5$  m. For both formulations, the model accurately reproduces the highly asymmetric water level variability on the reef flat. There is a slight underprediction of the reef water level for a brief period during the initial ebb phase of the tide ( $t \approx 3$  h), due to the presence of an along-reef component of the water level gradient during this period (see section 3.1) that is not captured in this simplified 1-D model. Nonetheless, this 1-D model does a remarkable job at reproducing the water levels observed both on and off the reef, and justifies using the model to investigate the dynamics of these tidal flows. Given that both the constant  $C_d$  and logarithmic  $k_s$  gave nearly the same results, we will now focus on results with the constant  $C_d$

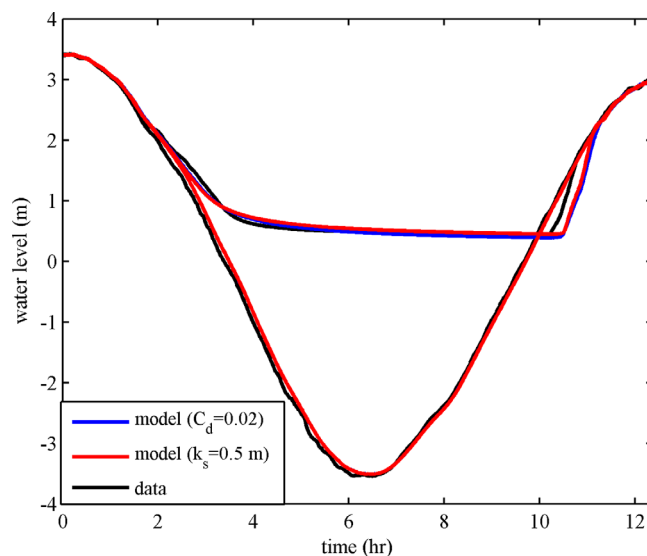


**Figure 8.** Comparison of the modeled versus observed water levels ( $\eta$ ) both on and the off reef platform, showing results for a tidal cycle on 2 April during the spring phase of the tide. Model results are shown using both a constant drag coefficient formulation with  $C_d = 0.02$  and a logarithmic formulation (equation (6)) using  $k_s = 0.5$  m. For the water level on the reef, the rms error of the prediction is 0.06 m and the skill is 0.99 for both drag formulations.

to the reef water level and propagates across the platform as a tidal bore (Figure 9i). In Figure 9 we also show the cross-reef variation in the local Froude number ( $Fr = u/\sqrt{gh}$ ) computed for these tidal phases. Although the flow is subcritical ( $Fr < 1$ ) across most of the reef platform during all phases of the tide, a critical flow point ( $Fr = 1$ ) emerges near the reef crest between  $t = 3$ – $4$  h until the tide begins to fill the reef once again (Figure 9).

#### 4.4. Momentum Balances

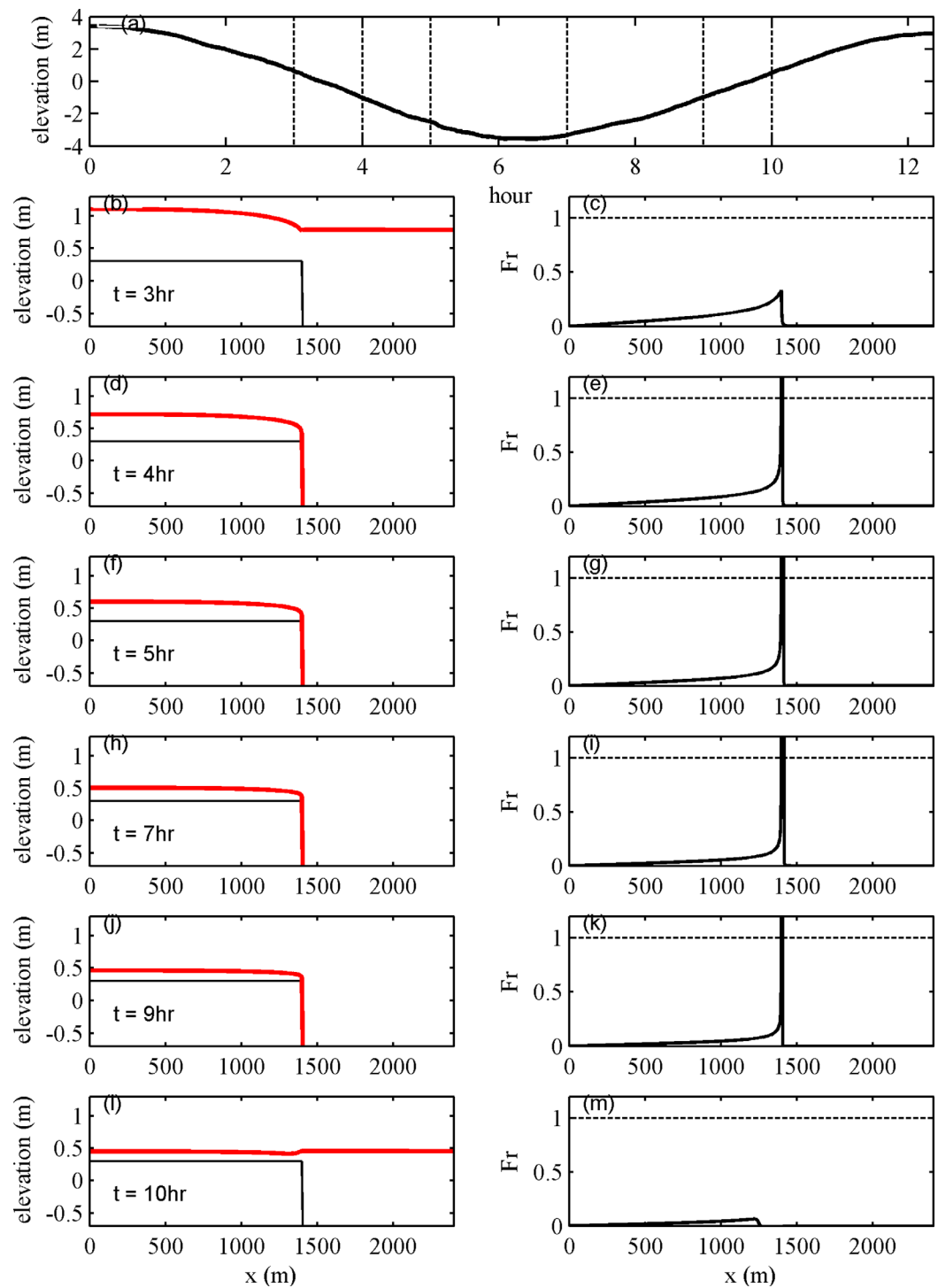
To investigate the dominant momentum balances established across the reef, each term in the nonlinear shallow water momentum equation (equation (4)) was locally computed and then spatially averaged across the reef platform from the shore to the reef crest (Figure 10). During the initial  $\sim 2$  h of the falling tide, all terms tend to be relatively weak. However, throughout the bulk of the tidal cycle ( $t \approx 2$ – $11$  h), a dominant momentum balance occurs between the pressure gradient driving the flow and the bed stress opposing it. While the horizontal advection term is not completely negligible during this period, it tends to always be  $< 10\%$  of the other dominant terms. Importantly, throughout this period the acceleration term ( $\partial u/\partial t$ ) is negligible, implying that the assumption of a quasi steady momentum balance on the reef is reasonable due to the slowly varying tide.

### 5. Analytical Solutions

While the full numerical solution of the momentum equation (equation (4)) can be used to accurately predict the hydrodynamics (e.g., with SWASH), these models must be developed for each reef application on a case-by-case basis, and most importantly do not directly reveal how the hydrodynamics are controlled by fundamental relationships between key system parameters such as reef morphology, bottom roughness, and tidal properties. Here we develop a set of analytical solutions to predict how water drains off the reef during ebb tide, as well as part of the flood tide when the offshore tidal level is still below the reef platform. Predicting the hydrodynamics during this period is the basis for understanding how much water will remain on a reef over a tidal cycle and, and most important to benthic organisms, whether a reef will become dry during low tide. In addition, water levels on the reef during the flood phase usually closely match offshore levels (see Figure 4), except for a brief ( $\sim 1$  h) pulse when the reef is initially flooded. As a consequence, the offshore water level alone can provide a very good approximation to the water level on the reef for the remaining part of the tidal cycle.

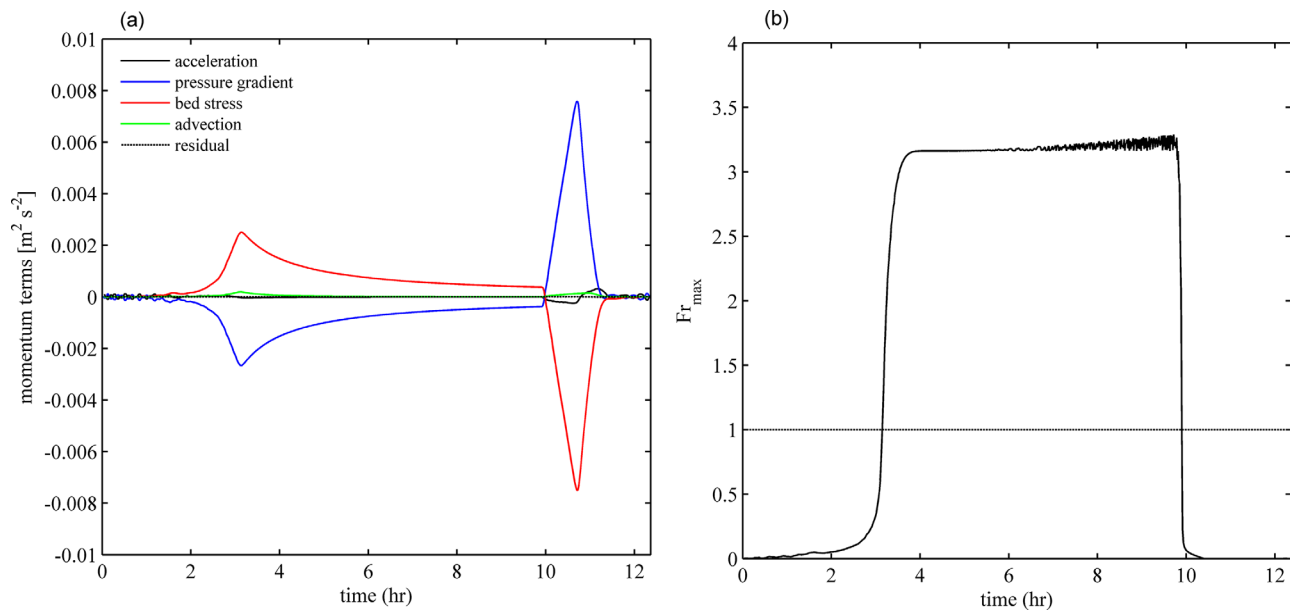
formulation for the remainder of the paper, as it can also be more readily incorporated into the analytical models developed below.

Figure 9 shows cross-reef profiles of the water levels ( $\eta$ ) at specific phases of the tide. By  $t = 3$  h the water level over the reef is clearly elevated relative to offshore, due to the reduction in the flow by bottom friction (Figure 9b). Slightly after  $t = 3$  h, the offshore water level falls below the platform yet the water depth at the back reef is still  $h \approx 0.8$  m (not shown). The reef water level continues to slowly fall (Figures 9d, 9f, 9h, and 9j), reaching a minimum value of  $h \approx 0.2$  m immediately before the offshore tide rises above the reef crest. As the reef platform is elevated ( $z_b = +0.3$  m) relative to MSL, the water level on the reef always remains above  $\eta \approx +0.5$  m. At  $t = 10$  h, the offshore water level becomes elevated relative



**Figure 9.** Cross-shore water level profiles ( $\eta$ ) at select phases of the offshore tide. (a) The offshore water levels with the tidal phases shown in the figures below as indicated by vertical-dashed lines. (left) Water levels  $\eta$  as red lines and bottom elevations  $z_b$  as black lines. (right) The corresponding Froude numbers of the flows at six phases of tide. (b) and (c)  $t = 3$  h; (d) and (e)  $t = 4$  h; (f) and (g)  $t = 5$  h; (h) and (i)  $t = 7$  h; (j) and (k)  $t = 9$  h; (l) and (m)  $t = 10$  h.

To simplify the problem, we focus on the part of the draining phase when the offshore water level is near or below the reef elevation. This is the  $\sim 7$  h period when the greatest deviation between the offshore and reef water levels occurs ( $+3 \text{ h} < t < +10 \text{ h}$ , Figure 4), and hence the period that is most important to predict. For this analysis, we assume that the dynamics are “quasi-steady” or equivalently that the local acceleration term in the momentum equation (equation (4)) is small relative to the other terms; one that was



**Figure 10.** (a) The spatially averaged momentum terms from equation (4), integrated on the reef platform from  $x = 0$  to  $x = L_r$ . Note that the bed slope term is zero on the reef platform, so is not shown. (b) The maximum Froude number  $Fr_{max}$  across the entire domain (including the forereef slope). Note that the horizontal dotted line denotes critical flow  $Fr = 1$ .

proven to be reasonable from the SWASH simulations (Figure 10a). By assuming quasi steady flow, mass conservation (equation (3)) allows us to assume that  $\partial h/\partial t$  is very small, and hence  $\partial q/\partial x$  is also very small. Under these assumptions, equation (5) can be expressed in the simple form [e.g., Akan, 2011]

$$\frac{dh}{dx} = \frac{S_0 - S_f}{1 - Fr^2}, \tag{7}$$

where  $S_0$  is the local bed slope and  $S_f$  is the friction slope defined as

$$S_f = \frac{\tau_b}{\rho gh} = \frac{C_d q^2}{gh^3}. \tag{8}$$

Equation (7) is the classic gradually varied flow equation for open channel flow and forms the basis of our analytical solutions.

Given that the flow on the reef platform is subcritical (hence controlled downstream), the solution of equation (7) requires a downstream boundary condition for  $h$  near the reef edge ( $x \approx L_r$ ). With the offshore water level at or below the platform, we can define two possible flow regimes (Figure 11): (1) a “normal flow regime,” where the flow everywhere remains subcritical (even down the forereef slope) and where the gravitational acceleration on the forereef slope is balanced by the bed stress; and (2) a “critical flow regime” where the flow becomes supercritical down the forereef slope and hence a critical flow point ( $Fr = 1$ ) occurs near the reef crest. Below we derive a solution for the normal flow case and show that the critical flow case can be treated as a special case of the more general normal flow solution.

Integrating mass conservation (equation (3)) across the reef by assuming no flow at the shoreline ( $x=0$ ) gives

$$\frac{d\mathcal{V}}{dt} = -q_{crest}, \tag{9}$$

where  $q_{crest}$  is the discharge at the reef edge and the storage  $\mathcal{V}$  is defined as the total volume of water per unit width on the reef:

$$\mathcal{V} \equiv \int_0^{L_r} h dx. \tag{10}$$



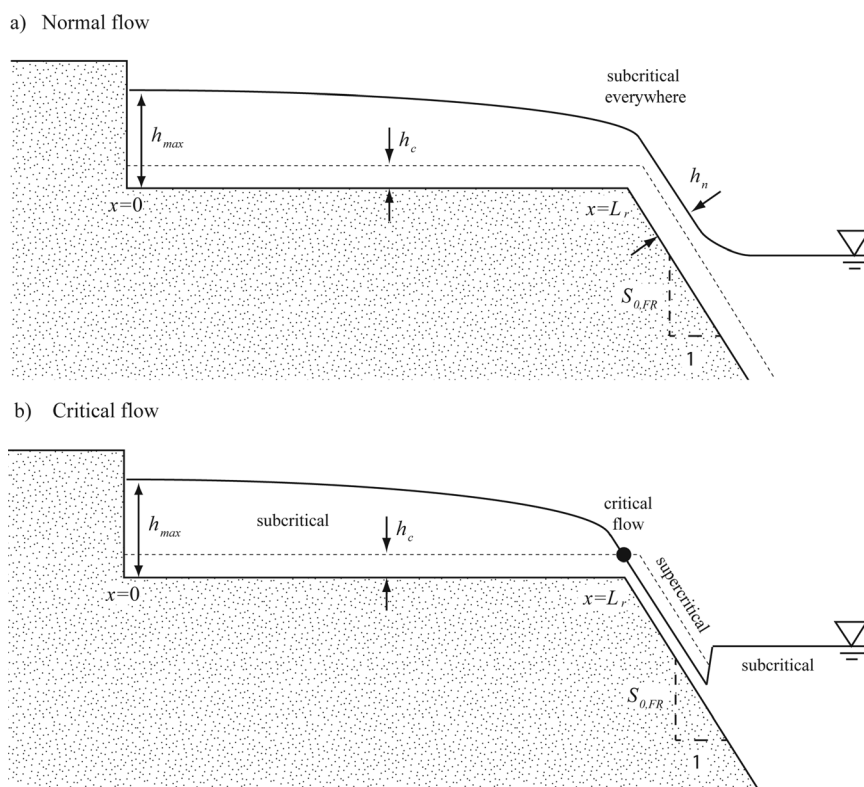


**Figure 11.** Two flow regimes for water draining off the reef when the offshore ocean water level is at or below the reef platform. (a) Regime 1, where the flow remains subcritical everywhere (i.e., the water depth  $h$  is everywhere greater than the critical depth  $h_c$ ). Normal flow conditions are established on the forereef slope, such that  $h$  is equal to the normal depth  $h_n$ . (b) Regime 2, where the flow is critical near the reef edge, separating sub and supercritical regions up and downstream, respectively. At the critical flow point, the local depth  $h$  matches the critical depth  $h_c$ . Note that  $S_{0,FR}$  denotes the forereef slope and is vertically exaggerated from the 1:5 slope assumed in the model.

We note that despite  $\partial q/\partial x$  being a small term,  $q$  must strictly vary from zero at the shoreline ( $x=0$ ) to  $q_{crest}$  at the reef edge ( $x=L_r$ ), since gradients in  $q$  are responsible for the falling reef water levels ( $\partial h/\partial t$ ) per equation (3). In the limit where  $\partial h/\partial t$  falls at a uniform rate across the reef,  $q$  should vary roughly linearly from  $x=0$  to  $L_r$ ,

$$q(x) = \frac{q_{crest}x}{L_r}, \quad (11)$$

This assumption of approximately linearly varying  $q$  across the reef is confirmed with the SWASH results in section 5.2 below.

For the case where the flow remains subcritical everywhere (Figure 11a), i.e., normal flow conditions down the forereef slope such that  $S_f = S_{0,FR}$ , the downstream boundary condition for  $h$  near the reef edge ( $x \approx L_r$ ) is the normal depth  $h_n$ :

$$h_n = \left( \frac{C_d q_{crest}^2}{S_{0,FR} g} \right)^{1/3}, \quad (12)$$

where  $S_{0,FR} = 0.2$  is taken as the slope of the Tallon forereef and we assume that  $C_d$  is constant everywhere. In Appendix A, we derive solutions for the water depth profile across the reef  $h(x)$  as a function of  $h_n$  (refer to equation (A7)), which when evaluated at the shoreline ( $x=0$ ) where the depth is  $h_{max}$  gives

$$\frac{h_{max}}{h_n} = \left( \frac{4 S_{0,FR} L_r}{3 h_n} \right)^{1/4}, \quad (13)$$

where we have assumed that  $S_{0,FR} L_r / h_n \gg 1$ . Likewise, the storage  $\Psi$  from equation (A14) is

$$\Psi = h_{\max} L_r - \frac{S_{0,FR} L_r^2}{12} \left( \frac{h_n}{h_{\max}} \right)^3 - \frac{S_{0,FR}^2 L_r^3}{42 h_n} \left( \frac{h_n}{h_{\max}} \right)^7. \tag{14}$$

The set of four equations (equations (9), (12), (13), and (14)) can thus be combined to predict how the water depth at the shoreline  $h_{\max}$  will decrease in time as we now show.

We start by rewriting equation (9) as

$$\frac{d\Psi}{dt} = \frac{d\Psi}{dh_n} \cdot \frac{dh_n}{dt} = - \left( \frac{g S_{0,FR}}{C_d} \right)^{1/2} h_n^{3/2}, \tag{15}$$

where  $q_{crest}$  on the right side has been replaced with equation (12). In equation (14), if we replace the functional dependency of  $h_n$  with  $h_{\max}$  using equation (13), an alternate form for  $\Psi$  is obtained:

$$\Psi = \Gamma S_{0,FR}^{1/4} L_r^{5/4} h_n^{3/4}, \tag{16}$$

where the constant  $\Gamma$  is given by

$$\Gamma \equiv \left( \frac{4}{3} \right)^{1/4} - \left( \frac{1}{12} \right) \left( \frac{3}{4} \right)^{3/4} - \left( \frac{1}{42} \right) \left( \frac{3}{4} \right)^{7/4} \approx 1.0. \tag{17}$$

By differentiating equation (16) to obtain  $d\Psi/dh_n$  in equation (15), and then integrating the initial value problem for  $h_n$  as a function of time, it can be shown that

$$\frac{h_n(t)}{h_{n,0}} = \frac{1}{\left( 1 + \left( \frac{S_{0,FR}}{C_d} \right)^{1/4} \frac{g^{1/2} h_{n,0}^{3/4}}{C_d^{1/4} L_r^{5/4}} t \right)^{4/3}}, \tag{18}$$

where  $h_{n,0}$  is the initial normal depth at the reef edge and we have assumed that  $\Gamma$  is exactly 1.0. Finally, we can use equation (13) to express equation (18) as a function of the shoreline depth  $h_{\max}$ :

$$\frac{h_{\max}(t)}{h_{\max,0}} = \frac{1}{1 + \left( \frac{3}{4} \right)^{1/4} \frac{t}{\Phi_f T_d}}, \tag{19}$$

where  $h_{\max,0}$  is the initial water level at the shoreline,  $T_d$  is a reef draining time-scale that is dependent on the width of the platform  $L_r$  and  $h_{\max,0}$ ,

$$T_d \equiv \frac{L_r}{(g h_{\max,0})^{1/2}}, \tag{20}$$

and  $\Phi_f$  is a dimensionless friction parameter defined as

$$\Phi_f \equiv \left( \frac{C_d L_r}{h_{\max,0}} \right)^{1/2}. \tag{21}$$

### 5.1. Critical Flow

When the foreereef slope is sufficiently steep, the flow down the slope may become supercritical ( $Fr > 1$ ) such that a critical flow point ( $Fr = 1$ ) must occur near the reef edge between the subcritical flow on the reef platform ( $Fr < 1$ ) (Figure 11b). For this case, the local water depth at the critical point is the critical depth  $h_c$  given by

$$h_c = \left( \frac{q_{crest}^2}{g} \right)^{1/3}. \tag{22}$$

This critical depth  $h_c$  is the minimum depth that can occur on the reef for a given  $q_{crest}$ . When comparing equation (12) for  $h_n$  with equation (22) for  $h_c$  it is clear that the flow at the reef edge will be subcritical everywhere if  $S_{0,FR} < C_d$  and will be critical if  $S_{0,FR} \geq C_d$ . Note that we can obtain a solution for the critical flow case where  $h_n = h_c$  by simply setting  $S_{0,FR} = C_d$  in the earlier normal flow solution. When this is done equation (18) becomes

$$\frac{h_c(t)}{h_{c,0}} = \frac{1}{\left( 1 + \frac{g^{1/2} h_{c,0}^{3/4}}{C_d^{1/4} L_r^{5/4}} t \right)^{4/3}}, \tag{23}$$

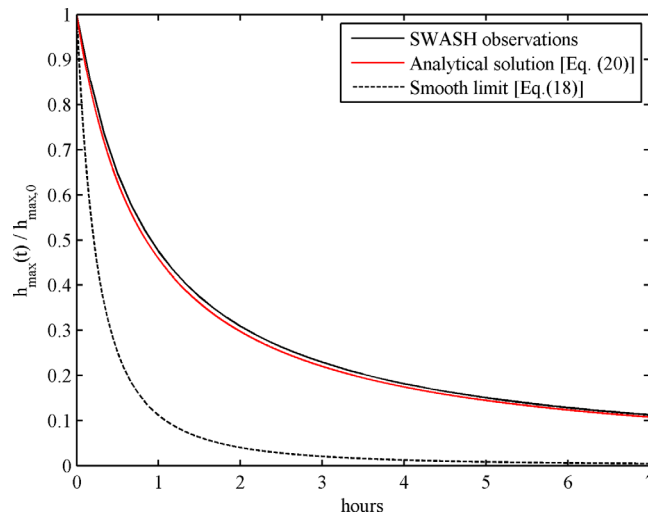


**Figure 12.** Decay in the normalized shoreline water depth  $h_{\max}(t)/h_{\max,0}$ , comparing the SWASH results with the analytical solution given by equation (19). The analytical solution for the smooth reef limit (equation (B3)) is also included for comparison.

where  $h_{c,0}$  is the initial value of  $h_c$ . The critical flow solution is thus predicted to be independent of the forereef slope  $S_{0,FR}$ , which physically makes sense as flow information downstream of the critical flow point can no longer propagate upstream. Most importantly, if we convert equation (23) to shoreline depths  $h_{\max}/h_{\max,0}$ , it can be shown that we obtain the identical solution to equation (19). Therefore, equation (19) has surprisingly broad applicability, independent of whether the flow becomes supercritical on the forereef slope or not. We emphasize that this is the case when  $C_d$  on the reef platform is the same as on the forereef; however, if the values differ substantially, the critical and normal flow solutions will differ, which is a hypothetical case we do not consider but can also be derived.

## 5.2. Analytical Model Predictions

The analytical model was applied using the identical parameters ( $L_r = 1400$  m,  $C_d = 0.02$ ) used in section 4.3 and initialized at the shoreline with the water depth in SWASH ( $h_{\max,0} \approx 1$  m) when the offshore water level fell below the crest at  $t = 3$  h. Figure 12 shows the time series of the decay in the normalized shoreline water depth  $h_{\max}(t)/h_{\max,0}$ , as computed with both SWASH and the analytical solution (equation (19)), with excellent agreement at all times. In Figure 12, the predicted decay of  $h_{\max}$  is also plotted for the smooth reef limit (refer to equation (B3) in Appendix B), revealing a substantial deviation. Given that the flow was critical at all times (see Figure 10b), it is clear that bottom friction contributes much more to maintaining elevated reef water levels than the hydraulic control mechanism, at least for this reef.

To investigate the sensitivity of the decay of  $h_{\max}$  to bottom drag, we conducted five additional SWASH simulations where  $C_d$  was varied over two orders of magnitude from 0.005 to 0.5 (Figure 13a). For each simulation, we compared the analytical model for the period commencing when  $h_{\max,0} = 1.0$  m, irrespective of whether the offshore water level had fallen completely below the crest. These variations in  $C_d$  have a substantial impact on the decay of  $h_{\max}$ . Most importantly, Figure 13a shows that the simple analytical solution for  $h_{\max}(t)/h_{\max,0}$  given by equation (19) agrees very well for all  $C_d$  values. Given that  $S_{0,FR} = 0.2$ , it is also important to emphasize that over this range of  $C_d$ , the flow at the edge of the reef varied from being critical ( $C_d \leq 0.2$ ) to subcritical ( $C_d > 0.2$ ) according to section 5.1, hence confirming that the model is indeed applicable over a wide range of flow regimes.

Likewise, we can also investigate how the water depth will decay on reefs having different widths  $L_r$ . In Figure 13b, we show SWASH model results for five values of  $L_r$  ranging between 200 and 2000 m, again initialized with  $h_{\max,0} = 1.0$  m, and compare these results to the analytical model. For the relatively wide reefs (i.e.,  $L_r \geq 1000$  m), the analytical model agrees very well with the SWASH simulations over the entire period. For the narrow reefs (i.e.,  $L_r \leq 600$  m), during the first  $\sim 1$  h the analytical model predicts that the depth should decay faster than was observed in the SWASH simulations. This initial discrepancy arises because for the narrow reef cases ( $L_r \leq 600$  m), local accelerations ( $\partial u/\partial t$ ) turn out to be important to the overall momentum balance when sea level initially starts falling; thus violating the quasi steady flow assumption in the model (not shown). Nonetheless, the analytical solutions converge to almost perfectly match the numerical solutions after  $\sim 1$  h and, most importantly, the analytical model is able to accurately predict the minimum depths that occur on the reefs at low tide for all reef widths. This latter result is particularly important for understanding what kind of habitats these intertidal platforms can provide and what kind of benthic communities they can support.

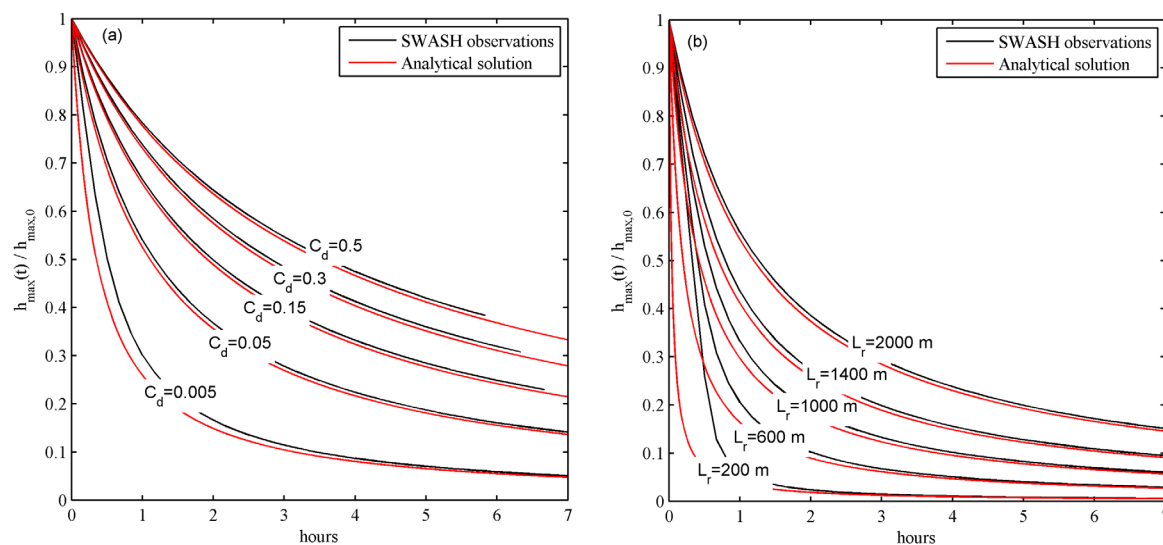


**Figure 13.** Effect of varying bottom drag coefficient  $C_d$  and reef width  $L_r$  on the reef water depth decay and comparison between the SWASH and analytical model results. (a) Effect of varying  $C_d$  with the reef width held constant at  $L_r = 1400$  m. (b) Effect of varying  $L_r$  (in meters) with the drag coefficient held constant at  $C_d = 0.02$ . For consistency, in all cases the analytical model comparison commences when  $h_{\max,0} = 1$  m.

## 6. Summary and Conclusions

The field observations revealed that the interaction of the large tides with the reef led to dramatic tidal water level asymmetries over each tidal cycle. During the flood phase, the reef platform rapidly filled, whereas water drained very slowly off the reef during ebb, causing the offshore water level to be several meters below the reef at low tide (Figure 4). As a consequence, the duration of the rising tide  $T_{\text{rise}}$  was only 2–3 h on the reef platform, versus 9–10 h for the falling tide  $T_{\text{fall}}$ . This is an extreme example of topographic tidal truncation, analogous to what can occur in strongly tidally forced estuaries due to topographic constrictions such as sills [e.g., *Lincoln and Fitzgerald, 1988; Warner et al., 2003*]. While similar dynamics have not been studied on shallow intertidal reef platforms, there have been some analogous observations in the Great Barrier Reef (GBR), e.g., at One Tree Island where the spring tidal range is mesotidal reaching  $\sim 2$  m [e.g., *Ludington, 1979; Wilson, 1985*]. These studies also observed large ebb duration asymmetries that were attributed to “ponding” of water within reef systems. Like many other coral cays in the GBR, the lagoon of One Tree Island is nearly completely enclosed by a narrow and shallow reef rim that restricts water from draining out of the lagoon during ebb tide. While the end effect on the tidal variability is similar, the “ponding” of water on the reef platform in the present study was largely due to the frictional resistance exerted by very wide and shallow reef platform rather than due to a topographic restriction of a shallow reef rim enclosing a deeper lagoon.

The large water level asymmetries on the reef platform also drove large velocity asymmetries. Thus, the period of offshore-directed flow during ebb lasted much longer than the onshore-directed flow during flood (Figure 5). In addition, the reef velocities were also influenced occasionally by along-reef water level gradients caused by the acceleration of the offshore flow as it curved around the reef island [e.g., *Geyer, 1993; Alae et al., 2004*]. Due to the orientation of the reef with respect to the tidal flow, the flow accelerated along the edge of the reef from south to north during ebb tide, leading to an  $\sim 1$ –2 h period following peak high tide where the along-reef water level gradient was not negligible (Figure 5). Averaged over the tidal cycle, however, this along-reef water level gradient led to a relatively weak residual discharge (typically  $< 0.2 \text{ m}^2 \text{ s}^{-1}$ ) directed northward on the reef (Figure 7). Nevertheless, once the offshore water level fell below the reef edge ( $\sim 3$  h after peak high tide), this along-reef water level vanished and the reef flow was no longer influenced by the offshore dynamics. Under these conditions, the flow was oriented uniformly in the cross-shore direction for the remaining  $\sim 7$  h of the ebb cycle on the reef.

Even with a brief period where the along-reef water level gradient was not negligible, we were able to successfully simulate the cross-reef water level variations over the entire tidal cycle using a 1-D numerical



model (SWASH). We found minimal differences in the model predictions when a depth-varying  $C_d$  was included (i.e., using a logarithmic formulation) rather than a constant  $C_d$ , so adopted a constant  $C_d = 0.02$  for Tallon reef that is also typical of values for other reef systems ( $\sim 0.01\text{--}0.05$ ; see *Lowe et al.* [2009b]). With this we were able to reproduce the observed asymmetric water level variability very well. The model output further revealed that the flow near the reef edge remained critical throughout the ebb, after the offshore water level fell below the reef crest. A detailed assessment of the momentum balances on the reef platform showed that there was a quasi steady momentum balance between local pressure gradients and bottom stresses across the reef, with only a very weak influence of horizontal advection term.

On this basis, a simple analytical model was developed to predict the decrease in water depth on the reef during ebb tide, which incorporated the effect of reef geometry, tidal range, bottom roughness, and fore-reef slope. In the model, we considered two flow regimes that set the downstream boundary condition: (1) where the flow became critical and (2) where the flow remained subcritical yet became fully developed down the forereef slope (i.e., normal flow). Interestingly, the solution for the normalized water depth decay at the shoreline  $h_{\max}(t)/h_{\max,0}$  was identical for both flow regimes (equation (19)) and was predicted to be independent of the forereef slope  $S_{0,FR}$  (also consistent with the SWASH observations). It should be noted that the critical flow case corresponds to the lower bound of the more general normal flow solution when the normal depth near the reef edge matches the critical depth; hence it is not surprising that the solutions are identical for both cases. When the water depth near the reef edge does become critical, the flow on the forereef can be either critical or supercritical. In both cases, the flow on the forereef downstream of the critical point does not influence the upstream flow on the reef platform.

Through the simple analytical model we found that the reef water depth decays as  $(t/\Phi_f T_d)^{-1}$ , where  $T_d$  is a reef draining time-scale (equation (20)) and  $\Phi_f$  is a dimensionless friction parameter (equation (21)). The model was able to accurately reproduce the water depth decay for a wide range of physically probable  $C_d$  and  $L_r$  values (Figure 13). These results can thus explain how very productive reef ecosystems living within the intertidal zone of reefs high above the offshore low tide elevation can remain submerged (and hence survive) over a full tidal cycle. For this present reef, bottom friction was most important in maintaining the reef water levels; i.e., the model predictions for the smooth reef limit ( $C_d=0$ ) showed that the water depth decays far too rapidly. Therefore, despite the presence of a critical flow point near the reef edge, analogous to the reef-rim control described in *Gourlay and Colleter* [2005], frictional head losses across the reef are so great that they still have a dominant influence on the rate water can discharge off the reef.

We can also use the analytical model to more generally explore the conditions (reef morphology, friction, and tidal properties) that are required to keep a reef platform submerged over a tidal cycle. For this, we consider a case where  $h_{\max,0} = 1$  m and that a reef becomes effectively “dry” if  $h_{\max} = \alpha h_{\max,0}$ , where  $\alpha$  denotes some fraction of the maximum depth. Although many reef organisms can survive within submerged depressions (e.g., small pools) on “dry” reefs, the ability for macrotidal platforms to support robust and diverse living benthic structures would be heavily dependent on their ability to maintain minimum water depths of at least the same scale as the maximum height of these organisms. Thus, by setting equation (19) equal to  $\alpha$ , we can calculate the time  $t_{dry}$  when the reef will become dry:

$$t_{dry} = \left(\frac{4}{3}\right)^{1/4} \left(\frac{1}{\alpha} - 1\right) \Phi_f T_d, \tag{24}$$

which predicts that  $t_{dry}$  will increase proportional to  $\Phi_f T_d$ . The offshore low tide duration lasts only  $0.5 T_{tide}$  (for a reef platform located near mean sea level), where  $T_{tide}$  varies from  $\sim 12$  h (dominantly semi-diurnal) to  $\sim 24$  h (dominantly diurnal). If we further assume that a reef is dry when  $\alpha=0.1$ , since many reef organisms (e.g., coral colonies, seagrasses, etc.) reach heights of order 0.1 m, a reef will dry under the following conditions: (1)  $\Phi_f T_d < 2200$  s (semidiurnal), or (2)  $\Phi_f T_d < 4400$  s (diurnal).

For the specific reef morphology in the present study, we have  $\Phi_f T_d \approx 2400$  s, thus very near (but just below) this drying threshold. If instead the tide was hypothetically diurnal at this site, the reef would become dry (in fact  $h_{\max}/h_{\max,0}$  would fall to  $< 0.02$  m  $\ll \alpha h_{\max,0}$ ). Thus, the biogenic formation and benthic community structure of intertidal reef platforms would also appear to be dependent on which particular tidal modes are dominant (semidiurnal versus diurnal) within a given region. Moreover, given that  $\Phi_f T_d$  increases as  $(C_d L_r^3)^{1/2}$ , it is important to emphasize that differences in the width of a reef  $L_r$  will proportionally have a much greater influence on reef draining than changes in  $C_d$ . Nevertheless, large (i.e., order of

magnitude) changes in  $C_d$  can clearly have an important influence on how much water remains on a reef each tidal cycle.

Although tide-dominated tropical reef systems are prevalent globally (with estimates suggesting they comprise up to 30% worldwide; see *Lowe and Falter* [2015]), detailed global assessments of the morphological properties of these reefs are lacking. This makes it difficult to know whether tide-dominated reefs are structured similarly to traditional wave-dominated fringing coral reefs, and thus how most of these reefs tend to fall within the parameter space of the analytical model. For example, on wave-dominated reefs, the relatively narrow range of wave forcing and reef morphology properties (i.e., reef widths, depths, and bottom roughness) implies that wave-driven flows are usually of order  $0.1 \text{ m s}^{-1}$  [*Falter et al.*, 2013]. Nevertheless, the tide-dominated platform reef at Tallon Island does share some general morphological features to wave-dominated fringing reefs, including the presence of a biogenically formed crest that separates the reef platform from a steep forereef slope [*Kennedy and Woodroffe*, 2002]. Thus, we expect that similar dynamics would also be operating on other tropical shallow reefs when the local tidal range is sufficiently large that the offshore water level falls below the crest at low tide. Given that the median depth of coral reef flats is  $\sim 1 \text{ m}$  [*Falter et al.*, 2013], this would suggest that reefs experiencing a tidal range  $> 2 \text{ m}$  would likely experience similar dynamics during at least some portion of their tidal cycle.

We must finally emphasize that while the trapping of water on a reef provides clear benefits for reef organisms in terms of avoiding aerial exposure, at the same it dramatically increases the residence (or flushing) times of reefs that can lead to extreme diel variations in water quality. For example, our recent field observations at Tallon Island indicate that daily temperature fluctuations can exceed  $10^\circ\text{C}$  when periods of sluggish flow on the reef (during low tides) occur around mid-day when light levels are maximal. Similarly, we have found that dissolved oxygen levels on the reef can vary between  $< 20\%$  saturation at night to  $> 200\%$  saturation each day, due to the respiration and production of the benthic reef communities during low phases of the tide. The extreme thermodynamic and biogeochemical variability that arise in these tide-dominated reefs will be explored in future studies.

### Appendix A: Analytical Solution for the Cross-Reef Water Depth Profile and Storage

From conservation of momentum, we apply equation (7), which for the region on the reef platform ( $x < L_r$ ) where  $S_o = 0$  gives:

$$\frac{dh}{dx} = \frac{-S_f}{1 - Fr^2}. \tag{A1}$$

The depth at the reef edge is the normal depth  $h_n$  given by equation (12), which depends on  $q_{crest}$  (Figure 11a). With  $q(x)$  varying linearly across the reef via equation (11), the local Froude number  $Fr$  can be expressed as a function of  $h_n$ :

$$Fr^2 = \frac{S_{0,FR}}{C_d} \left(\frac{x}{L_r}\right)^2 \left(\frac{h_n}{h}\right)^3. \tag{A2}$$

Likewise,  $S_f$  can be expressed as:

$$S_f = S_{0,FR} \left(\frac{x}{L_r}\right)^2 \left(\frac{h_n}{h}\right)^3. \tag{A3}$$

equation (A1) can be rearranged as

$$\left[\frac{1}{S_f} - \frac{Fr^2}{S_f}\right] dh = -dx, \tag{A4}$$

or when substituting equations (A2) and (A3) as

$$\left[\frac{C_d}{S_{0,FR}} \left(\frac{h}{h_n}\right)^3 - \left(\frac{x}{L_r}\right)^2\right] dh = -C_d \left(\frac{x}{L_r}\right)^2 dx. \tag{A5}$$

In section 5.1, we distinguished between two flow regimes: a normal flow condition when  $S_{0,FR} < C_d$ , and a critical flow condition when  $S_{0,FR} \geq C_d$  and the ratio  $C_d/S_{0,FR}$  is set to 1 in equation (A5).

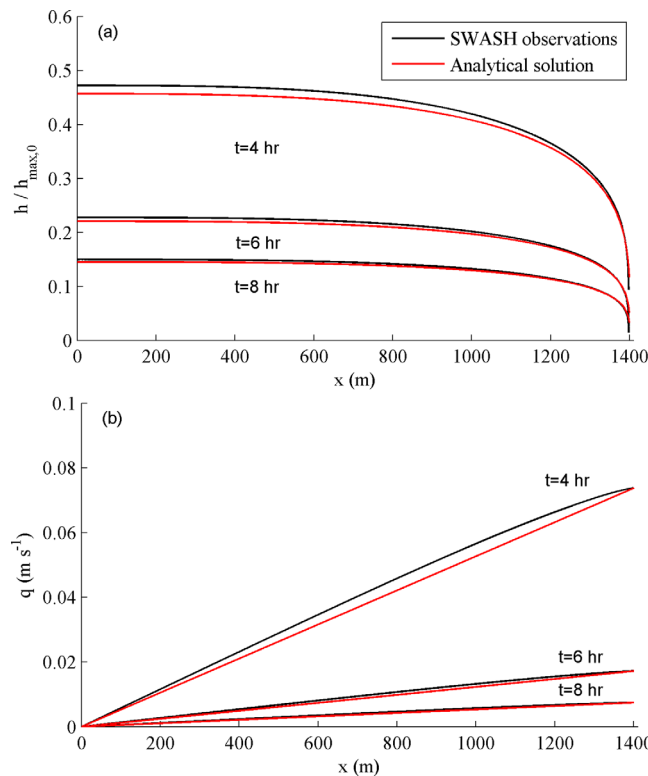


**Figure A1.** (a) The normalized water depth profile  $h(x)/h_{\max,0}$  across the reef at three times ( $t = 4, 6$  and  $8$  h), comparing SWASH results with the analytical solution given by equation (A7). The initial water depth  $h_{\max,0} = 0.83$  m is taken as the shoreline depth when the offshore water level falls below the reef platform. (b) Variations in discharge  $q(x)$  across the reef comparing SWASH with the analytical solution given by equation (11).

Therefore, for both cases, the second term on the left side of equation (A5) has a negligible effect on the volume of water stored on the reef platform when it is sufficiently wide, since over most of the reef  $(x/L_r)^2 \ll (C_d/S_{0,FR})(h/h_n)^3$ , which we confirm below. Thus, integrating from an arbitrary point  $x$  on the reef to the edge (at  $x=L_r$ ) we obtain

$$\int_h^{h_n} \left(\frac{h}{h_n}\right)^3 dh = -S_{0,FR} \int_x^{L_r} \left(\frac{x}{L_r}\right)^2 dx, \tag{A6}$$

which can be rearranged to give a solution for the water depth variation  $h(x)$  across the reef

$$\frac{h(x)}{h_n} = \left[ 1 + \frac{4 S_{0,FR} L_r}{3 h_n} \left( 1 - \left(\frac{x}{L_r}\right)^3 \right) \right]^{1/4}. \tag{A7}$$

Although it may appear from equation (A7) that the water level profile is independent of  $C_d$ , we note that the normal depth  $h_n$  is itself dependent on  $C_d$  per equation (12).

To compute the storage  $\Psi$ , equation (A7) must be integrated across the reef using equation (10). As

there is no simple analytical solution, we develop an approximate solution by first writing equation (A7) as

$$h(x) = h_n [R - Px^3]^{1/4}, \tag{A8}$$

where

$$R \equiv 1 + \frac{4 S_{0,FR} L_r}{3 h_n} \tag{A9}$$

and

$$P \equiv \frac{4 S_{0,FR}}{3 h_n L_r^2} \tag{A10}$$

The function given by equation (A8) can be expressed as a Taylor series expansion about  $x = 0$  as

$$\frac{h(x)}{h_n} = R^{1/4} - \frac{Px^3}{4R^{3/4}} - \frac{3P^2x^6}{32R^{7/4}} + O[x^8], \tag{A11}$$

where only the first three nonzero terms are shown. Equation (10) then becomes

$$\Psi = h_n \int_0^{L_r} \left[ R^{1/4} - \frac{Px^3}{4R^{3/4}} - \frac{3P^2x^6}{32R^{7/4}} \right] dx, \tag{A12}$$

which when rearranging and noting that

**Table A1.** Comparison of the Prediction of Storage  $\Psi$  at Three Phases of the Tide, Using the Numerical Integration of the SWASH Results, the Numerical Integration of the Analytical Water Depth Profile From equation (A7), and the Approximate Explicit Form Given by Equation (A14)

	t = 4 h	t = 6 h	t = 8 h
$\Psi$ (SWASH) (m <sup>2</sup> )	496	239	157
$\Psi$ (equation (A7)) (m <sup>2</sup> )	483	233	153
$\Psi$ (equation (A14)) (m <sup>2</sup> )	491	237	156

$$\frac{h_{\max}}{h_n} = R^{1/4} \tag{A13}$$

when using equation (A8) with  $h=h_{\max}$  at  $x=0$ , gives

$$\Psi = h_{\max} L_r - \frac{S_{0,FR} L_r^2}{12} \left( \frac{h_n}{h_{\max}} \right)^3 - \frac{S_{0,FR}^2 L_r^3}{42 h_n} \left( \frac{h_n}{h_{\max}} \right)^7 \tag{A14}$$

Equation (A14) gives an expression for  $\Psi$  as a function of the water depth at the reef edge ( $h_n$ ) and the shoreline ( $h_{\max}$ ).

To assess the analytical prediction of the reef water depth profile (equation (A7)) and storage  $\Psi$  (equation (A14)), we assume the model parameters described in section 5.2. Figure A1a shows three snapshots in time of the water depth profile computed across the reef using SWASH, compared with the analytical solution (equation (A7)). There is excellent agreement, with only a very small difference ( $\sim 3\%$ ) in  $h_{\max}$  at  $t = 4$  h in the worst case. Likewise, at each time there is very good agreement between the storage  $\Psi$  computed with SWASH and that obtained with the analytical solution (equation (A14), Table ). Figure A1b also shows the spatial variation in discharge  $q$  across the reef computed with SWASH and with the analytical model (equation (11)). This confirms that the scaling arguments predicting a linear variation in  $q$  across the reef is appropriate, with only a very small (sublinear) deviation in SWASH initially at  $t = 4$  h.

### Appendix B: Analytical Solution for the Smooth Reef Limit

In the smooth reef limit where  $C_d \ll 1$ , equation (7) predicts  $dh/dx=0$ ; therefore, the water level profile on the reef is effectively flat such that  $h(x)=h_{\max}$  everywhere. By using the momentum equation on the reef platform (equation (A1)), for the smooth reef limit, we have  $S_f=0$  implying  $dh/dx=0$  (i.e., the water surface is flat on the reef platform), thus eliminating the usefulness of the solution in Appendix A for this case. By instead using the conservation of energy equation (not shown), one can show that [e.g., Akan, 2011]

$$h_{\max} = \frac{3}{2} h_c \tag{B1}$$

We note that spatial variability in  $q$  is not important in this smooth reef limit case since the bottom stress across the reef is zero irrespective of the flow. From mass conservation (equation (9)), we thus have

$$\frac{dh_{\max}}{dt} = -\frac{q}{L_r} = -\left(\frac{2}{3}\right)^{3/2} \frac{g^{1/2}}{L_r} h_{\max}^{3/2} \tag{B2}$$

Integrating equation (B2) subject to the initial condition  $h_{\max,0}$  at  $t = 0$  gives

$$\frac{h_{\max}(t)}{h_{\max,0}} = \frac{1}{\left[1 + \frac{1}{2} \left(\frac{2}{3}\right)^{3/2} \frac{t}{T_d}\right]^2} \tag{B3}$$

where  $T_d$  is the same draining time-scale defined in equation (20).

### References

Akan, A. O. (2011), *Open Channel Hydraulics*, 364 pp., Butterworth-Heinemann, Burlington, Mass.  
 Alaei, M. J., G. Ivey, and C. Pattiaratchi (2004), Secondary circulation induced by flow curvature and Coriolis effects around headlands and islands, *Ocean Dyn.*, 54(1), 27–38.  
 Becker, J., M. Merrifield, and M. Ford (2014), Water level effects on breaking wave setup for Pacific Island fringing reefs, *J. Geophys. Res. Oceans*, 119, 914–932, doi:10.1002/2013JC009373.  
 Bonneton, P., J.-P. Lefebvre, P. Bretel, S. Ouillon, and P. Douillet (2007), Tidal modulation of wave-setup and wave-induced currents on the Aboré coral reef, New Caledonia, *J. Coast. Res.*, 50, 762–766.  
 Callaghan, D. P., P. Nielsen, N. Cartwright, M. R. Gourlay, and T. E. Baldock (2006), Atoll lagoon flushing forced by waves, *Coastal Eng.*, 53(8), 691–704, doi:10.1016/j.coastaleng.2006.02.006.  
 Dumas, F., R. Le Gendre, Y. Thomas, and S. Andréfouët (2012), Tidal flushing and wind driven circulation of Ahe atoll lagoon (Tuamotu Archipelago, French Polynesia) from in situ observations and numerical modelling, *Mar. Pollut. Bull.*, 65(10), 425–440.

### Acknowledgments

This project was funded by the Western Australia Marine Science Institution (WAMSI) as part of the WAMSI Kimberley Marine Research Program, and an ARC Future Fellowship grant (FT110100201) to R.J.L. We thank Nick Mortimer for the major role he played in the field work for this study, as well as Carlin Bowyer for assistance with the bathymetric data analysis. We are especially grateful for the field assistance and guidance provided by the Bardi Jawi Rangers in One Arm Point, as well as the Bardi Jawi people through their advice and consent to access their traditional lands. Thanks also to the Kimberley Marine Research Station for their support of the field logistics. Finally, we thank Marcel Zijlema for providing the *Stelling and Duinmeijer* [2003] test case for SWASH and general advice on the model for this application, as well as feedback from two anonymous reviewers that helped to improve the manuscript. The data presented in this article are archived on UWA's Institutional Research Data Store (IRDS) and can be requested by contacting R. Lowe (Ryan.Lowe@uwa.edu.au).

- Falter, J. L., R. J. Lowe, Z. Zhang, and M. McCulloch (2013), Physical and biological controls on the carbonate chemistry of coral reef waters: Effects of metabolism, wave forcing, sea level, and geomorphology, *PLoS One*, *8*(1), e53303.
- Gerritsen, F. (1980), Wave attenuation and wave set-up on a coastal reef, *Coastal Eng. Proc.*, *1*(17), 444–461.
- Geyer, W. R. (1993), Three-dimensional tidal flow around headlands, *J. Geophys. Res.*, *98*(C1), 955–966.
- Goring, D. G., and V. I. Nikora (2002), Despiking acoustic Doppler velocimeter data, *J. Hydraul. Eng.*, *128*(1), 117–126.
- Gourlay, M. (1996), Wave set-up on coral reefs. 1. Set-up and wave-generated flow on an idealised two dimensional horizontal reef, *Coastal Eng.*, *27*(3), 161–193.
- Gourlay, M. R., and G. Colleter (2005), Wave-generated flow on coral reefs: An analysis for two-dimensional horizontal reef-tops with steep faces, *Coastal Eng.*, *52*(4), 353–387, doi:10.1016/j.coastaleng.2004.11.007.
- Hardy, T. A., and I. R. Young (1996), Field study of wave attenuation on an offshore coral reef, *J. Geophys. Res.*, *101*(C6), 14,311–14,326.
- Hench, J. L., J. J. Leichter, and S. G. Monismith (2008), Episodic circulation and exchange in a wave-driven coral reef and lagoon system, *Limnol. Oceanogr.*, *53*(6), 2681–2694.
- Jago, O., P. Kench, and R. Brander (2007), Field observations of wave-driven water-level gradients across a coral reef flat, *J. Geophys. Res.*, *112*, C06027, doi:10.1029/2006JC003740.
- Kench, P. (1998), Physical processes in an Indian Ocean atoll, *Coral Reefs*, *17*(2), 155–168.
- Kennedy, D., and C. Woodroffe (2002), Fringing reef growth and morphology: A review, *Earth Sci. Rev.*, *57*(3), 255–277.
- King, B., and E. Wolanski (1996), Tidal current variability in the central Great Barrier Reef, *J. Mar. Syst.*, *9*(3), 187–202.
- Kowalik, Z. (2004), Tide distribution and tapping into tidal energy, *Oceanologia*, *46*(3), 291–331.
- Lincoln, J. L., and D. M. Fitzgerald (1988), Tidal distortions and flood dominance at five small tidal inlets in southern Maine, *Mar. Geol.*, *82*(3), 133–148.
- Lowe, R. J., and J. L. Falter (2015), Oceanic forcing of coral reefs, *Ann. Rev. Mar. Sci.*, *7*(1), 43–66, doi:10.1146/annurev-marine-010814-015834.
- Lowe, R. J., J. L. Falter, M. D. Bandet, G. Pawlak, M. J. Atkinson, S. G. Monismith, and J. R. Koseff (2005), Spectral wave dissipation over a barrier reef, *J. Geophys. Res.*, *110*, C04001, doi:10.1029/2004JC002711.
- Lowe, R. J., J. L. Falter, S. G. Monismith, and M. J. Atkinson (2009a), A numerical study of circulation in a coastal reef-lagoon system, *J. Geophys. Res.*, *114*, C06022, doi:10.1029/2008JC005081.
- Lowe, R. J., J. L. Falter, S. G. Monismith, and M. J. Atkinson (2009b), Wave-driven circulation of a coastal reef-lagoon system, *J. Phys. Oceanogr.*, *39*(4), 873–893.
- Ludington, C. (1979), Tidal modifications and associated circulation in a platform reef lagoon, *Mar. Freshwater Res.*, *30*(4), 425–430.
- Lugo-Fernandez, A., H. Roberts, and W. Wiseman Jr. (1998a), Tide effects on wave attenuation and wave set-up on a Caribbean coral reef, *Estuarine Coastal Shelf Sci.*, *47*(4), 385–393.
- Lugo-Fernández, A., H. H. Roberts, and J. N. Suhayda (1998b), Wave transformations across a Caribbean fringing-barrier coral reef, *Cont. Shelf Res.*, *18*(10), 1099–1124.
- McDonald, C., J. Koseff, and S. Monismith (2006), Effects of the depth to coral height ratio on drag coefficients for unidirectional flow over coral, *Limnol. Oceanogr.*, *51*(3), 1294–1301.
- Monismith, S. G. (2007), Hydrodynamics of coral reefs, *Annu. Rev. Fluid Mech.*, *39*, 37–55.
- Monismith, S. G., L. M. Herdman, S. Ahmerkamp, and J. L. Hench (2013), Wave transformation and wave-driven flow across a steep coral reef, *J. Phys. Oceanogr.*, *43*(7), 1356–1379.
- Nelson, R. C. (1994), Depth limited design wave heights in very flat regions, *Coastal Eng.*, *23*(1), 43–59.
- Nidzieko, N., and D. Ralston (2012), Tidal asymmetry and velocity skew over tidal flats and shallow channels within a macrotidal river delta, *J. Geophys. Res.*, *117*, C03001, doi:10.1029/2011JC007384.
- Pomeroy, A., R. Lowe, G. Symonds, A. Van Dongeren, and C. Moore (2012), The dynamics of infragravity wave transformation over a fringing reef, *J. Geophys. Res.*, *117*, C11022, doi:10.1029/2012JC008310.
- Purcell, S. (2002), Intertidal reefs under extreme tidal flux in Buccaneer Archipelago, Western Australia, *Coral Reefs*, *21*(2), 191–192.
- Roeber, V., and K. F. Cheung (2012), Boussinesq-type model for energetic breaking waves in fringing reef environments, *Coastal Eng.*, *70*, 1–20.
- Sheremet, A., J. Kaihatu, S.-F. Su, E. Smith, and J. Smith (2011), Modeling of nonlinear wave propagation over fringing reefs, *Coastal Eng.*, *58*(12), 1125–1137.
- Stelling, G., and S. Duijnmeijer (2003), A staggered conservative scheme for every Froude number in rapidly varied shallow water flows, *Int. J. Numer. Methods Fluids*, *43*(12), 1329–1354.
- Symonds, G., K. P. Black, and I. R. Young (1995), Wave-driven flow over shallow reefs, *J. Geophys. Res.*, *100*(C2), 2639–2648.
- Taebi, S., R. J. Lowe, C. B. Pattiaratchi, G. N. Ivey, G. Symonds, and R. Brinkman (2011), Nearshore circulation in a tropical fringing reef system, *J. Geophys. Res.*, *116*, C02016, doi:10.1029/2010JC006439.
- Van Dongeren, A., R. Lowe, A. Pomeroy, D. M. Trang, D. Roelvink, G. Symonds, and R. Ranasinghe (2013), Numerical modeling of low-frequency wave dynamics over a fringing coral reef, *Coastal Eng.*, *73*, 178–190.
- Vetter, O., J. Becker, M. Merrifield, A. C. Pequignet, J. Aucan, S. Boc, and C. Pollock (2010), Wave setup over a Pacific Island fringing reef, *J. Geophys. Res.*, *115*, C12066, doi:10.1029/2010JC006455.
- Warner, J., D. Schoellhamer, and G. Schladow (2003), Tidal truncation and barotropic convergence in a channel network tidally driven from opposing entrances, *Estuarine Coastal Shelf Sci.*, *56*(3), 629–639.
- Willmott, C. J. (1982), Some comments on the evaluation of model performance, *Bull. Am. Meteorol. Soc.*, *63*(11), 1309–1313.
- Wilson, P. (1985), Tidal studies in the One Tree Island lagoon, *Mar. Freshwater Res.*, *36*(2), 139–156.
- Zhou, J., and P. Stansby (1999), 2D shallow water flow model for the hydraulic jump, *Int. J. Numer. Methods Fluids*, *29*(4), 375–387.
- Zijlema, M., G. Stelling, and P. Smit (2011), SWASH: An operational public domain code for simulating wave fields and rapidly varied flows in coastal waters, *Coastal Eng.*, *58*(10), 992–1012.